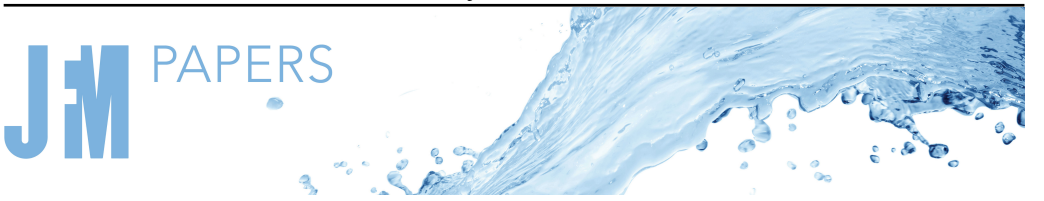
J. Fluid Mech. (2026), *vol.* 1036, A66, doi:10.1017/jfm.2026.11662



Derivation of a consistent shallow-flow model for viscoplastic fluids and application to the dam-break problem and flow stoppage

Danila Denisenko[1], **Gaël Loïc Richard**[1] **and Guillaume Chambon**[1]

[1]Univ. Grenoble Alpes, INRAE, CNRS, IRD, Grenoble INP, IGE, 38000 Grenoble, France

Corresponding author: Danila Denisenko, d.denisenko.hydro@gmail.com

(Received 30 October 2025 UTC; revised 17 April 2026 UTC; accepted 6 May 2026 UTC)

A consistent three-equation shallow-flow model is derived for Herschel–Bulkley fluids propagating down an inclined plane. A rigorous asymptotic method is used to incorporate the complex rheological properties of the material into the model. Difficulties arise from the coexistence inside the flow of a sheared layer, in which the material is largely above the yielding threshold, and a pseudoplug layer, in which the material is just on the verge of yielding. The derivation of the model is based on two steps. First, the flow variables are expanded up to the first order of accuracy in terms of flow aspect ratio, in both the sheared and the pseudoplug layers. A specific generalization of the tensorial constitutive law is proposed, allowing us to implement a regular perturbation method in the entire domain. Second, the mass, momentum and energy balance equations are formally averaged over the flow depth. This results in three coupled equations for the fluid depth, the average velocity and a third variable, the enstrophy, related to the internal shearing of the flow. The final model has the structure of a fully hyperbolic system with relaxation source terms, and is adapted to represent dry fronts and material stoppage. A linear stability analysis is performed, showing a stabilizing effect of plasticity in good agreement with experimental results. A simple well-balanced numerical scheme is proposed, and various flow configurations are simulated, including roll waves and dam-break problems. The relative influences of plasticity, shear-thinning and shearing in the pseudoplug are investigated.

Key words: shallow water flows, general fluid mechanics, non-Newtonian flows

© The Author(s), 2026. Published by Cambridge University Press. This is an Open Access article, distributed under the terms of the Creative Commons Attribution licence (https://creativecommons.org/licenses/by/4.0/), which permits unrestricted re-use, distribution and reproduction, provided the original article is properly cited.

https://doi.org/10.1017/jfm.2026.11662 Published online by Cambridge University Press

1. Introduction

Viscoplastic fluids are materials that behave as a solid body as long as the stress remains below the yield stress, and as a viscous fluid above this threshold. Many geophysical mass flows such as avalanches, mud and lava flows involve yield-stress behaviour (Ancey 2007). Biological materials such as blood clots or mucus can be viscoplastic, causing relevant problems in medicine (Balmforth, Frigaard & Ovarlez 2014). Engineering applications such as inkjet printing, the creation of chocolate confections or concrete, all have to deal with the viscoplastic behaviour (Bird *et al.* 1983). In this work, we consider free-surface flows of idealized viscoplastic fluids down an inclined plane under gravity. Here, idealized viscoplasticity corresponds to a perfectly rigid behaviour in the solid-like regime.

Mathematical modelling of ideal viscoplastic fluid flows generally relies on the Bingham or the Herschel–Bulkley constitutive laws, combined with mass conservation and Cauchy momentum equations. An accurate direct numerical simulation of this problem generally requires large computing times and the use of very fine meshes in the vicinity of yield surfaces separating unyielded (solid-like) from yielded (fluid-like) regions (Frigaard & Nouar 2005; Glowinski & Wachs 2011; Dimakopoulos, Pavlidis & Tsamopoulos 2013; Liu, Balmforth & Hormozi 2019). Alternatively, approximate models of reduced dimensionality can be considered. For free-surface flows, a thin-layer approximation combined with an integration over the flow depth is the most common approach to derive reduced models. In addition to reducing the number of equations to be solved, this approach also allows the boundary conditions to be directly incorporated into the models.

The thin-layer approach includes one-equation models based on a single mass balance equation (Balmforth *et al.* 2006; Ancey & Cochard 2009) and more general shallow-flow models relying on two (Ng & Mei 1994; Fernández-Nieto *et al.* 2010; Muchiri, Monnier & Sellier 2025) or three equations (Denisenko, Richard & Chambon 2023). One-equation models have usually simple structures and are easy to implement, however, they might produce diverging or inaccurate solutions when the instability threshold for uniform flows is exceeded (Benney 1966; Pumir, Manneville & Pomeau 1983; Ooshida 1999). Two-equation shallow-flow models include inertia and are widely used for many types of fluids. They are typically based on the mass and momentum balance equations. However, these models are generally incompatible with the work–energy theorem (Richard *et al.* 2019). This issue can be overcome by using three-equation shallow-flow models, which are usually based on mass, momentum and energy balance equations. Compatibility with the work–energy theorem is guaranteed by the introduction of an enstrophy variable, related to internal shearing of the flow. This approach was initially proposed by Teshukov (2007) and successfully applied to viscous fluids by Richard, Ruyer-Quil & Vila (2016), to Bingham materials by Denisenko *et al.* (2023) and to granular materials by Deleage & Richard (2025). An important advantage of this three-equation approach is the fully hyperbolic structure of the resulting models, which ensures the well-posedness of the problem and allows for efficient computational resolution with robust numerical schemes.

The key parameter in thin-layer approaches is the aspect ratio $\varepsilon = h_0/l_0$, where h_0 and l_0 are the typical depth and length of the flow, respectively. Thin-layer models are derived by averaging the governing equation along the depth, using asymptotic expansions with respect to ε. To capture the right physics and properly account for the fluid rheology, the derived models should be consistent at least at order $O(\varepsilon)$. A model is said to be consistent at order k if the leading terms in the model equations are of $O(1)$, and if all terms vanish except for a remainder of $O(\varepsilon^{k+1})$ after having inserted the asymptotic expansions obtained above into the model equations. Many consistent models have been derived for Newtonian (Benney 1966; Ruyer-Quil & Manneville 2000; Usha & Uma 2004; Richard

https://doi.org/10.1017/jfm.2026.11662 Published online by Cambridge University Press

et al. 2016) or power-law fluid flows (Ruyer-Quil, Chakraborty & Dandapat 2012; Noble & Vila 2013; Boutounet, Monnier & Vila 2016; Chesnokov 2021). However, the derivation of consistent models for viscoplastic fluids remains rare (Balmforth & Liu 2004; Fernández-Nieto *et al.* 2010; Denisenko *et al.* 2023) and is limited to the case of Bingham fluids. Extension of these models to Herschel–Bulkley fluids is challenging due to an additional singularity in the viscous stress tensor and the nonlinear behaviour inherent to power-law rheology. Yet, the Herschel–Bulkley model is better representative of real viscoplastic materials, making such extensions essential for realistic modelling.

Most models used in practical applications for viscoplastic fluids are inconsistent and generally based on simple, *ad hoc* closures. In particular, the friction term is often postulated from the relation associated with the leading-order velocity profile. For Bingham fluids, this leads to an analytical expression of the friction term (Huang & Garcia 1998). However, this expression depends on the unknown position of the yield surface. Pastor *et al.* (2004) expressed this position as a function of the friction, providing a closure more suitable for numerical implementation under the form of a third-order polynomial. For Herschel–Bulkley fluids, this approach leads to a nonlinear algebraic equation that cannot be solved analytically (Ancey, Andreini & Epely-Chauvin 2012). An analytical fit for this equation was proposed by Coussot (1997) for values of power-law index n close to $1/3$. Muchiri *et al.* (2025) proposed considering a friction term linearly dependent on the velocity. It allows them to write the friction term in an analytical form, but their expression does not coincide with the exact expression of the friction term in the particular case of power-law fluids (Ng & Mei 1994). Generally, inconsistent *ad hoc* shallow-flow models may demonstrate relatively accurate predictions for the front velocity and free-surface shape (Hogg & Pritchard 2004; Ancey & Cochard 2009; Ancey *et al.* 2012; Saingier, Deboeuf & Lagrée 2016; Fernández-Nieto *et al.* 2023; Muchiri *et al.* 2024). However, these models usually fail to capture the proper instability threshold of the equilibrium flows (Balmforth & Liu 2004; Kalliadasis *et al.* 2012).

The main difficulty in deriving consistent shallow-flow models for Herschel–Bulkley fluids is related to the intricacies of the asymptotic expansion. At leading order with respect to ε, the velocity expansion describes a yielded layer at the base of the flow, overlaid by a rigid plug close to the free surface (Coussot 1994; Chambon, Ghemmour & Laigle 2009). However, at the next order, this plug layer happens to be a pseudoplug in which the strain rate is of order $O(\varepsilon)$ (Balmforth & Craster 1999; Chambon *et al.* 2020). The strain rate thus derived diverges at the interface between the pseudoplug and the sheared layer, resulting in a non-smooth velocity profile. While it is possible to employ this expansion for deriving a consistent shallow-flow model (Fernández-Nieto *et al.* 2010), this model is characterized by a complex mathematical structure and exhibits an unphysical destabilizing effect of plasticity at large angles, predicting an absolutely unstable rigid layer at the plastic limit (Denisenko *et al.* 2023). A smooth expression for the velocity field, avoiding divergence of the strain rate, can be obtained through an asymptotic matching procedure that introduces an additional transition layer and includes extra terms of higher orders (Fernández-Nieto *et al.* 2010; Denisenko, Richard & Chambon 2025). However, these extra terms are given by non-integrable expressions, preventing one from deriving a traceable shallow-flow model. In our recent paper (Denisenko *et al.* 2025) we proposed an alternative path to construct a smooth velocity expansion given by fully analytical expressions, based on an alternative tensorial extension of the Herschel–Bulkley law. In the case of Bingham fluids, this approach was already successfully used to derive a three-equation shallow-flow model with a good mathematical structure (Denisenko *et al.* 2023).

https://doi.org/10.1017/jfm.2026.11662 Published online by Cambridge University Press

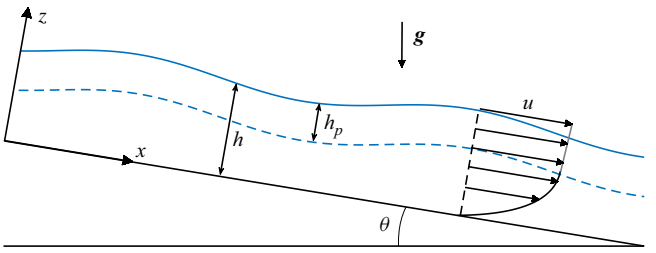


Figure 1. Definition sketch.

The goal of this paper is to derive a consistent three-equation shallow-flow model based on the alternative tensorial extension of the Herschel–Bulkley law. The three-equation approach of Richard *et al.* (2016) is important to get the compatibility with the depth-averaged energy equation, while employing the new asymptotic expansion of Denisenko *et al.* (2025) is crucial to obtain a physical instability threshold. The model is derived by averaging the mass, momentum and energy equations. The final result is a hyperbolic system with relaxation source terms, allowing robust numerical schemes to be employed. The influence of the yield-stress and shear-thinning effects on the instability criterion and roll waves are investigated. Importantly, the model is adapted to handle dry fronts and stoppage of the material. These properties are generally lacking in existing consistent shallow-flow models. Comparisons with dam-break experiments are performed. The final plastic shapes of the fluid are studied.

The structure of the paper is the following. In § 2, we present the alternative tensorial extension of the Herschel–Bulkley constitutive law and formulate the governing equations for the fluid flow motion. In § 3, we provide the expression for the long-wave asymptotic expansion ensuring a smooth velocity field. In § 4, a consistent three-equation shallow-flow model is derived from the asymptotic expansion. Section 5 presents applications to various flow configurations, including uniform flow instability, the dam-break problem and flow stoppage. Lastly, in § 6, the influence of selecting different source terms is examined by comparing results for steady-state surges.

2. Statement of the problem

We study a two-dimensional gravity-driven flow of a viscoplastic fluid down an inclined plane (figure 1). The angle of the plane to the horizontal is denoted by θ. The gravity vector is $\boldsymbol{g}$. The x- and z-axes are parallel and orthogonal to the plane, respectively. The components of the velocity $\boldsymbol{v}$ along the x and z directions are denoted u and w. The components of the strain-rate tensor $\dot{\boldsymbol{\gamma}}$ are defined as $\dot{\gamma}_{xx} = 2\partial u/\partial x$, $\dot{\gamma}_{xz} = \partial u/\partial z + \partial w/\partial x$, $\dot{\gamma}_{zz} = 2\partial w/\partial x$. The fluid depth is denoted by $h(x, t)$. The fluid is incompressible ($\mathrm{tr}\,\dot{\boldsymbol{\gamma}} = 0$) with a density ρ and a pressure p.

2.1. *Constitutive law*

A generalized tensorial extension of the Herschel–Bulkley constitutive law within the framework of the shallow-flow asymptotic expansion has been proposed in our recent work (Denisenko *et al.* 2025). Namely, the extra-stress tensor $\boldsymbol{\tau}$ is expressed as

$$\tau_{ij} = \tau_{ij}^{Y} + K|\dot{\boldsymbol{\gamma}}|^{n-1}\dot{\gamma}_{ij} \qquad |\dot{\boldsymbol{\gamma}}| > 0, \tag{2.1}$$

$$\dot{\gamma}_{ij} = 0 \qquad |\boldsymbol{\tau}| \leqslant \tau_c. \tag{2.2}$$

https://doi.org/10.1017/jfm.2026.11662 Published online by Cambridge University Press

The parameters K and n are the consistency and the power index of the material, respectively. The tensor $\boldsymbol{\tau}^Y$ is called the yield-stress tensor. The norm is defined as $|\boldsymbol{T}| = (0.5\boldsymbol{T}_{ij}\boldsymbol{T}_{ij})^{0.5}$ for any second-order tensor. Hereinafter, for $|\boldsymbol{\tau}| > \tau_c$, we split the extra-stress in its yield-stress and viscous contributions as

$$\tau_{ij} = \tau_{ij}^Y + \tau_{ij}^v, \quad \tau_{ij}^v = K\dot{\gamma}_{ij}|\dot{\boldsymbol{\gamma}}|^{n-1}. \tag{2.3}$$

Unlike in the classical tensorial extension of the Herschel–Bulkley rheology, here the yield-stress tensor is not assumed to be aligned with the strain-rate tensor via the expression $\tau_{ij}^Y = \tau_c\dot{\gamma}_{ij}/|\dot{\boldsymbol{\gamma}}|$. We instead define the yield-stress tensor $\boldsymbol{\tau}^Y$ based on the following criteria.

(i) The norm of $\boldsymbol{\tau}^Y$ is equal to the yield stress τ_c in the yielded regime: $|\boldsymbol{\tau}^Y| = \tau_c$. This corresponds to the von Mises yielding criterion.
(ii) The trace of $\boldsymbol{\tau}^Y$ is zero in relation to the incompressibility assumption: $\mathrm{tr}\,\boldsymbol{\tau}^Y = 0$.
(iii) There are no normal stress differences in simple shear, such that $\boldsymbol{\tau}^Y$ is aligned with $\dot{\boldsymbol{\gamma}}/|\dot{\boldsymbol{\gamma}}|$ in the particular case of simple shear flows. Although questionable, this assumption is made to obtain the same leading-order solution as in models based on the classical formulation of the rheology.
(iv) The existence of a normal stress difference in the pseudoplug at leading order (see below), and all terms originating from these normal stresses in the asymptotic expansions at $O(\varepsilon)$, are attributed to the yield-stress tensor and not to the viscous-stress tensor $\tau^v = K\dot{\gamma}|\dot{\boldsymbol{\gamma}}|^{n-1}$. All other terms in the asymptotic expansions are attributed to the viscous-stress tensor.

The constitutive law (2.1) together with these four conditions can be viewed as an alternative extension of the one-dimensional Herschel–Bulkley law for two-dimensional shallow flows, since the classical scalar expression $\tau_{xz} = \tau_c + \dot{\gamma}^n$ is recovered in simple-shear flows. The fourth condition here can be interpreted as a closure assumption ensuring that the normal stress differences associated with the perfectly rigid regime do not influence the fluid-like dynamics. It avoids the spurious destabilizing effects of plasticity at large slope angles that are observed in the model based on the classical tensorial law (Denisenko *et al.* 2023). It is important to emphasize that the four conditions formulated above are meaningful only in the shallow-flow regime, where a dominant direction can be identified and the flow is close to one-dimensional. Although these conditions are not sufficient to fully determine the yield-stress tensor in a general flow, they are sufficient to work out a thin-layer asymptotic expansion up to $O(\varepsilon)$.

The conditions on τ_{ij}^Y formulated above were first proposed in Denisenko *et al.* (2023) to avoid the singularity of the yield-stress tensor for $|\dot{\boldsymbol{\gamma}}| = 0$. This allowed us to derive a consistent three-equation shallow-flow model for Bingham fluids with a smooth velocity field and a physically correct instability threshold. Later these conditions were used in the derivation of a smooth asymptotic expansion for Herschel–Bulkley fluids (Denisenko *et al.* 2025). Here we build on these previous developments to derive a consistent three-equation shallow-flow model in the Herschel–Bulkley case.

2.2. *Governing equations*

The continuity equation (mass conservation balance) reads

$$\frac{\partial u}{\partial x} + \frac{\partial w}{\partial y} = 0. \tag{2.4}$$

https://doi.org/10.1017/jfm.2026.11662 Published online by Cambridge University Press

The Cauchy momentum equations in the x and z directions read

$$\rho\left(\frac{\partial u}{\partial t}+u\frac{\partial u}{\partial x}+w\frac{\partial u}{\partial z}\right)=-\frac{\partial p}{\partial x}+\rho g\sin\theta+\frac{\partial \tau_{xz}}{\partial z}+\frac{\partial \tau_{xx}}{\partial x}, \tag{2.5}$$

$$\rho\left(\frac{\partial w}{\partial t}+u\frac{\partial w}{\partial x}+w\frac{\partial w}{\partial z}\right)=-\frac{\partial p}{\partial z}-\rho g\cos\theta+\frac{\partial \tau_{xz}}{\partial x}+\frac{\partial \tau_{xx}}{\partial z}. \tag{2.6}$$

At the bottom, no-penetration and no-slip boundary conditions are assumed:

$$u_{|z=0}=w_{|z=0}=0. \tag{2.7}$$

At the free surface, the kinematic boundary condition is given by

$$\frac{\partial h}{\partial t}+u_{|z=h(x)}\frac{\partial h}{\partial x}=w_{|z=h(x)}, \tag{2.8}$$

while the dynamic boundary conditions are

$$\left[1-\left(\frac{\partial h}{\partial x}\right)^2\right]\tau_{xz|z=h(x)}=2\left(\frac{\partial h}{\partial x}\right)\tau_{xx|z=h(x)}, \tag{2.9}$$

$$\left[1-\left(\frac{\partial h}{\partial x}\right)^2\right]p_{|z=h(x)}=-\left[1+\left(\frac{\partial h}{\partial x}\right)^2\right]\tau_{xx|z=h(x)}. \tag{2.10}$$

Note that capillarity is neglected in this study. The atmospheric pressure is taken constant and equal to zero.

2.3. *Shallow-flow scaling*

Let us denote by h_0 the characteristic length in z direction, by l_0 the characteristic length in x direction and by u_0 the characteristic velocity in x direction. The shallow-flow hypothesis implies that the aspect ratio $\varepsilon=h_0/l_0$ is small. The relevant dimensionless groups of the problem are the Reynolds number Re, the Froude number Fr and the Bingham number Bi:

$$Re=\frac{\rho u_0^{2-n}h_0^n}{K},\qquad Fr=\frac{u_0}{\sqrt{gh_0\cos\theta}},\qquad Bi=\frac{\tau_c}{K}\left(\frac{h_0}{u_0}\right)^n. \tag{2.11}$$

In this study, these parameters and the slope angle θ are assumed to be $O(1)$ with respect to ε. To rewrite the problem (2.4)–(2.10) into a dimensionless form, the flow variables are expressed as

$$x=l_0x';\quad z=h_0z';\quad u=u_0u';\quad w=\varepsilon u_0w';\quad t=\frac{l_0}{u_0}t';\quad h=u_0h';$$
$$p=\rho gh_0\cos\theta\,p';\quad \tau_{ij}=\tau_c\tau'_{ij};\quad |\boldsymbol{\tau}|=\tau_c|\boldsymbol{\tau}'|;\quad |\dot{\boldsymbol{\gamma}}|=\frac{u_0}{h_0}|\dot{\boldsymbol{\gamma}}'|. \tag{2.12}$$

For convenience, we shall further omit the primes. The continuity (2.4) keeps the form

$$\frac{\partial u}{\partial x}+\frac{\partial w}{\partial y}=0, \tag{2.13}$$

while the scaled momentum (2.5)–(2.6) take the following form:

https://doi.org/10.1017/jfm.2026.11662 Published online by Cambridge University Press

$$\varepsilon\left(\frac{\partial u}{\partial t}+u\frac{\partial u}{\partial x}+w\frac{\partial u}{\partial z}\right)=-\frac{\varepsilon}{Fr^2}\frac{\partial p}{\partial x}+\frac{\lambda}{Re}+\frac{Bi}{Re}\frac{\partial \tau_{xz}}{\partial z}+\frac{\varepsilon Bi}{Re}\frac{\partial \tau_{xx}}{\partial x}, \tag{2.14}$$

$$\varepsilon^2\left(\frac{\partial w}{\partial t}+u\frac{\partial w}{\partial x}+w\frac{\partial w}{\partial z}\right)=-\frac{1}{Fr^2}\left(1+\frac{\partial p}{\partial z}\right)+\frac{\varepsilon Bi}{Re}\frac{\partial \tau_{xz}}{\partial x}+\frac{Bi}{Re}\frac{\partial \tau_{zz}}{\partial z}, \tag{2.15}$$

with the driving parameter λ given by

$$\lambda=\frac{\rho g h_0^{n+1}\sin\theta}{K u_0^n}=\frac{Re}{Fr^2}\tan\theta. \tag{2.16}$$

In the scaled variables, the yielding criterion reduces to $|\boldsymbol{\tau}|=1$. For $|\boldsymbol{\tau}|>1$, the expressions for the viscous and yield-stress components of (2.3) are transformed to

$$\tau_{xx}=\tau_{xx}^Y+\tau_{xx}^v, \qquad \tau_{xx}^v=\frac{2\varepsilon}{Bi}\frac{\partial u}{\partial x}|\dot{\boldsymbol{\gamma}}|^{n-1}, \tag{2.17}$$

$$\tau_{xz}=\tau_{xz}^Y+\tau_{xz}^v, \qquad \tau_{xz}^v=\frac{1}{Bi}\left(\frac{\partial u}{\partial z}+\varepsilon^2\frac{\partial w}{\partial x}\right)|\dot{\boldsymbol{\gamma}}|^{n-1}. \tag{2.18}$$

The condition on the norm of the dimensionless yield-stress tensor is

$$\left(\tau_{xx}^Y\right)^2+\left(\tau_{xz}^Y\right)^2=1. \tag{2.19}$$

The no-penetration and no-slip conditions (2.7) keep the same form,

$$u_{|z=0}=w_{|z=0}=0, \tag{2.20}$$

while the scaled kinematic and dynamic boundary conditions (2.8)–(2.10) are rewritten as

$$\frac{\partial h}{\partial x}+u_{|z=h(x)}\frac{\partial h}{\partial x}=w_{|z=h(x)}, \tag{2.21}$$

$$\left[1-\varepsilon^2\left(\frac{\partial h}{\partial x}\right)^2\right]\tau_{xz|z=h(x)}=2\varepsilon\left(\frac{\partial h}{\partial x}\right)\tau_{xx|z=h(x)}, \tag{2.22}$$

$$\left[1-\varepsilon^2\left(\frac{\partial h}{\partial x}\right)^2\right]p_{|z=h(x)}=-\frac{BiFr^2}{Re}\left[1+\varepsilon^2\left(\frac{\partial h}{\partial x}\right)^2\right]\tau_{xx|z=h(x)}. \tag{2.23}$$

Finally, the norms of the dimensionless stress and strain-rate tensors read

$$|\boldsymbol{\tau}|=\sqrt{\tau_{xx}^2+\tau_{xz}^2}, \qquad |\dot{\boldsymbol{\gamma}}|=\sqrt{\left(\partial_z u+\varepsilon^2\partial_x w\right)^2+4\varepsilon^2\left(\partial_x u\right)^2}. \tag{2.24}$$

3. Asymptotic expansion

Asymptotic expansions of the flow variables for the alternative rheology (2.1)–(2.2) have been derived up to $O(\varepsilon)$ in our recent paper (Denisenko *et al.* 2025). All variables are expanded as

$$f=f^{(0)}+\varepsilon f^{(1)}+O(\varepsilon^2). \tag{3.1}$$

The detailed expressions of these expansions are given in Appendix A. Here we only recall the structure and key properties of the longitudinal velocity expansion.

At leading order, the term $u^{(0)}$ coincides with the expression obtained for the classical Herschel–Bulkley constitutive law, as considered in many studies (e.g. Coussot 1994; Chambon *et al.* 2009). It corresponds to a sheared layer at the base of the flow, overlaid

https://doi.org/10.1017/jfm.2026.11662 Published online by Cambridge University Press

by a rigid plug close to the free surface. The thickness of the plug is $h_p = Bi/\lambda$. In this plug the stress is at the yielding point $|\boldsymbol{\tau}| = \tau_c$ due to the contribution of the plastic normal stresses. At the next order, the plug layer is treated as a pseudoplug, characterized by a strain rate of order $O(\varepsilon)$. This idea was proposed by Balmforth & Craster (1999) in order to allow the asymptotic expansion to be carried out.

At first order, the correction $u^{(1)}$ consists of two contributions. The first contribution is identical to the result derived for the classical Herschel–Bulkley constitutive law under the assumption of zero shearing in the pseudoplug, obtained by Balmforth & Liu (2004). The second contribution depends on an additional parameter δ and arises as a result of the 'Bingham plateau' regularization, which is introduced at $O(\varepsilon)$ for $n < 1$ in order to suppress the divergence of the local effective viscosity and to allow for non-zero shearing in the pseudoplug. This regularization is required to obtain asymptotic expansions in a closed analytical form with the alternative tensorial constitutive law used here, and only concerns the viscous stress tensor, such that the material remains perfectly rigid below the yielding threshold (for more details see Denisenko *et al.* (2025)). Importantly, applying this regularization at $O(\varepsilon)$, rather than at $O(1)$, is beneficial, as it does not affect the leading-order expression and allows us to recover the classical Herschel–Bulkley result for $u^{(0)}$. The regularization parameter δ is considered to be small and of order $O(\varepsilon^{\beta})$ with $\beta > 0$, so the total contribution associated with δ is of $O(\delta^{1/n-1}\varepsilon) = O(\varepsilon^{1+\beta(1/n-1)})$ and it does not formally contribute to the expansions up to $O(\varepsilon)$.

In essence, the parameter δ allows one to tune the magnitude of a small shear rate in the pseudoplug. In particular, a suitable value of this parameter enables an accurate approximation of the 'complete' asymptotic expansion associated with non-integrable equations (for more details see Denisenko *et al.* (2025)). However, as shown later, the effect of this parameter on the instability thresholds and free-surface profiles is barely noticeable.

It should also be noted that the definition of the yield-stress tensor $\boldsymbol{\tau}^Y$ through the four conditions (i)–(iv) can thus be considered as a specific type of regularization written in the framework of shallow flows. Indeed, it recovers the classical shallow-flow asymptotic expansion in the fully sheared layer up to $O(\varepsilon)$; the differences arise only in the pseudoplug region at $O(\varepsilon)$. However, unlike classical regularizations – where solid behaviour is approximated by a highly viscous fluid – the material here remains truly rigid below the yield point. As a result, the present approach for deriving the tractable asymptotic expansion of viscoplastic fluids combines two distinct types of regularization: one avoids the singularity of the yield-stress tensor by relaxing the general collinearity condition between the yield-stress tensor and the strain-rate tensor and replacing it with additional closure assumptions that allow to preserve the rigid behaviour below the yield point; the other modifies the power-law viscous contribution at $O(\varepsilon)$ in the pseudoplug layer by replacing Herschel–Bulkley behaviour with Bingham behaviour, while retaining the full Herschel–Bulkley rheology at leading order.

4. Depth-averaged model

The model is derived by averaging the governing (2.13)–(2.15) over the flow depth, taking into account the boundary conditions at the bottom and at the free surface. The asymptotic expansions presented in the Appendix A are used for neglecting all terms smaller than $O(\varepsilon\delta^{1/n-1})$. It should be emphasized that an infinite number of asymptotically consistent models with different source terms can be derived using the asymptotic procedure presented below. However, not all such formulations would lead to physically meaningful or numerically robust solutions. The selection of appropriate source terms

https://doi.org/10.1017/jfm.2026.11662 Published online by Cambridge University Press

requires physically motivated judgement beyond formal asymptotic consistency. This point is particularly highlighted in § 6, where we demonstrate that different formulations of the source terms result in markedly different steady-state surge solutions. In fact, the choice of source terms adopted in our paper was reached after exploring a range of possible formulations and selecting the one that best satisfies physical and numerical considerations.

For any flow variable A, we define the depth-averaged value $\langle A\rangle$ by

$$\langle A\rangle = \frac{1}{h}\int_0^h A\mathrm{d}z. \tag{4.1}$$

For the averaged longitudinal velocity, we use the specific notation $\langle u\rangle = U$. The expression for the leading-order term $U^{(0)}$ comes readily from (A5):

$$U^{(0)} = \frac{n}{1+2n}\lambda^{\frac{1}{n}}h^{\frac{n+1}{n}}\left(1-\frac{h_p}{h}\right)^{\frac{n+1}{n}}\left(1+\frac{n}{n+1}\frac{h_p}{h}\right). \tag{4.2}$$

4.1. *Mass conservation*

Averaging the continuity (2.13) and taking into account the kinematic boundary condition (2.21) yields the following mass conservation equation:

$$\frac{\partial h}{\partial t}+\frac{\partial hU}{\partial x}=0. \tag{4.3}$$

Inserting the leading-order asymptotic expansion (4.2) for U into (4.3) results in a kinematic wave equation:

$$\frac{\partial h}{\partial t}+\lambda^{\frac{1}{n}}h(h-h_p)^{\frac{1}{n}}\frac{\partial h}{\partial x}=\mathrm{O}(\varepsilon). \tag{4.4}$$

This equation, together with the expressions of $u^{(1)}$ given by (A11)–(A17), allows us to write the first-order correction $U^{(1)}$ in the form given by (A18) in Appendix A.

4.2. *Momentum balance*

The momentum balance (2.14) is averaged over the depth, using the no-slip condition (2.20), the kinematic boundary condition (2.21) and the dynamic boundary conditions (2.22) and (2.23). Employing the leading-order expressions for the stresses (A1)–(A4) and for the pressure (A6), yields

$$\frac{\partial}{\partial t}(hU)+\frac{\partial}{\partial x}\left(h\langle u^2\rangle+\frac{h^2}{2Fr^2}\right)=-\frac{Bi\tau_{xz}^{(1)}(0)}{Re}+O(\varepsilon), \tag{4.5}$$

where $\tau_{xz}^{(1)}(0)$ denotes the first-order correction to the shear stress at the bottom $z=0$.

In most shallow-flow models, the quadratic term $\langle u^2\rangle$ is replaced by U^2, so the mass conservation (4.3) and the momentum balance (4.5) yield a system of two coupled equations for the flow height h and the depth-averaged velocity U. This assumption is justified if the fluid is only slightly sheared. However, in general viscous fluids this is not the case. To treat properly the term $\langle u^2\rangle$, we introduce the deviation of the velocity from its averaged value:

$$u^*(x,z,t)=u(x,z,t)-U(x,t). \tag{4.6}$$

https://doi.org/10.1017/jfm.2026.11662 Published online by Cambridge University Press

By definition $\langle u^* \rangle = 0$, so that $\langle u^2 \rangle = U^2 + \langle u^{*2} \rangle$ in (4.5). The deviation $\langle u^{*2} \rangle$ could be formally estimated by the asymptotic expansion at leading order. This would yield a closed system of two coupled equations for the variables h and U (Fernández-Nieto *et al.* 2010; Noble & Vila 2013). However, as shown by Richard *et al.* (2019) for viscous fluids, to guarantee the compatibility of the averaged mass and momentum equations with the depth-averaged energy equation, one should rather consider the deviation $\langle u^{*2} \rangle$ as an independent variable (see also Teshukov 2007). We adapt here this three-variable approach for Herschel–Bulkley fluids. Instead of $\langle u^{*2} \rangle$, it is more convenient to introduce the following third variable:

$$\varphi = \frac{\langle u^{*2} \rangle}{h(h - h_p)}. \tag{4.7}$$

This variable φ plays the role of an entropy for the system (Richard & Gavrilyuk 2012) and is called enstrophy. The negative correction term $-h\,h_p$ in the denominator of (4.7) is required only in the viscoplastic case, in order to prevent a non-physical relaxation of the enstrophy towards zero at $h = h_p$ later in the model.

The expansion of the enstrophy,

$$\varphi = \varphi^{(0)} + \varepsilon \varphi^{(1)} + O(\varepsilon^2), \tag{4.8}$$

leads to $\varphi^{(0)} = \left\langle (u^{*(0)})^2 \right\rangle / h(h - h_p)$ and $\varphi^{(1)} = 2\langle u^{*(0)} u^{*(1)} \rangle / h(h - h_p)$. Thus, at leading order we have

$$\varphi^{(0)} = \frac{\lambda^{\frac{2}{n}} h^{\frac{2}{n}} n^3}{(2n+1)^2(3n+2)} (1 - \xi)^{\frac{2(1+n)}{n}} \left(1 + \frac{3n+2}{(n+1)^2} n\xi \right). \tag{4.9}$$

Here $\xi = h_p / h$. At order $O(\varepsilon)$ the expression $\varphi^{(1)}$ is lengthy and given by (A19) in Appendix A.

Introducing the new variable φ, (4.5) is rewritten as

$$\frac{\partial}{\partial t}(hU) + \frac{\partial}{\partial x}\left(hU^2 + h^3\varphi + \frac{h^2}{2Fr^2} \right) = -\frac{Bi\,\tau_{xz}^{(1)}(0)}{Re} + \frac{\partial}{\partial x}\left(h_p h^2 \varphi \right). \tag{4.10}$$

To derive a model with a well-posed mathematical structure, the source terms on the right-hand side of (4.10) should be expressed as a sum of relaxation terms for h, U and φ. Using the relation (4.4), the shear stress correction (A9) and the expression (A18) for $U^{(1)}$, one can write

$$\frac{Bi\,\tau_{xz}^{(1)}(0)}{Re} = \frac{3n(n+1)(2n+1)}{3n\left[2n\xi\,(n\xi+1) + n + 1\right](1-\xi)^{\frac{1}{n}} + \zeta^{\frac{1-n}{n}}(n+1)(2n+1)} \frac{U^{(1)}}{\lambda^{\frac{1-n}{n}} h^{\frac{1}{n}} Re} - \lambda^{\frac{2}{n}} h^{\frac{2(1+n)}{n}} C_1(n, \xi, \zeta) \frac{\partial h}{\partial x}, \tag{4.11}$$

where the function C_1 is given in Appendix B and the dimensionless quantity ζ is defined as $\zeta = \delta / h$. The second term on the right-hand side of (4.10) can be expressed at leading order using (4.9):

$$\frac{\partial}{\partial x}\left(h_p h^2 \varphi \right) = \lambda^{\frac{2}{n}} h^{\frac{2(1+n)}{n}} C_2(n, \xi) \frac{\partial h}{\partial x} + O(\varepsilon). \tag{4.12}$$

Here the function C_2 is given in Appendix B.

We can now express the different terms in (4.11) and (4.12) using forms that relax towards the equilibrium (leading-order) solution. For the first term in (4.11), using the

https://doi.org/10.1017/jfm.2026.11662 Published online by Cambridge University Press

asymptotic expansion $U = U^{(0)} + \varepsilon U^{(1)} + O(\varepsilon^2)$ and expression (4.2) for $U^{(0)}$, we can write

$$\lambda h[1 - q(n,\xi)] - Bi - \alpha_1(n)\frac{U}{h}\left|\frac{U}{h}\right|^{n-1} = \\ -\frac{\varepsilon}{\lambda^{\frac{1-n}{n}} h^{\frac{1}{n}}}\left[(2n+1)(1-\xi)^{n-\frac{1}{n}}\left(\frac{n+1}{n\xi+n+1}\right)^{1-n}\right]U^{(1)} + O(\varepsilon^2) \tag{4.13}$$

where α_1 and q are given by

$$\alpha_1(n) = \left(\frac{2n+1}{n}\right)^n, \quad q(n,\xi) = (1-\xi)\left[1 - \left(\frac{(1-\xi)(n\xi+n+1)}{n+1}\right)^n\right]. \tag{4.14}$$

Accordingly, the quantity $U^{(1)}$ can be written as a relaxation term in U:

$$U^{(1)} = -\frac{\lambda^{\frac{1-n}{n}} h^{\frac{1}{n}}(1-\xi)^{\frac{1-n^2}{n}}(n+1)^{n-1}}{\varepsilon(2n+1)(n\xi+n+1)^{n-1}}\left[\lambda h[1-q(n,\xi)] - Bi - \alpha_1(n)\frac{U}{h}\left|\frac{U}{h}\right|^{n-1}\right]. \tag{4.15}$$

The derivative $\partial h/\partial x$ in (4.11) and (4.12) can be expressed consistently as the sum of two relaxation terms in U and φ. First, let us consider the following relation obtained from the asymptotic expansions for U and φ:

$$\varphi^{\frac{n-2}{2}}\left[\varphi - \alpha_2(n,\xi)\frac{U^2}{h^2}\right] = \varepsilon Re\lambda^{\frac{2}{n}} h^{\frac{2(1+n)}{n}} C_3(n,\xi,\zeta)\frac{\partial h}{\partial x} + \varepsilon\frac{C_4(n,\xi,\zeta)}{\lambda^{\frac{1-n}{n}} h^{\frac{1}{n}}}U^{(1)} + O(\varepsilon^2). \tag{4.16}$$

Here the functions C_3 and C_4 are given in Appendix B, while the function α_2 reads

$$\alpha_2(n,\xi) = n\frac{n[(3n+2)\xi + n + 2] + 1}{(3n+2)(n\xi+n+1)^2}. \tag{4.17}$$

From (4.2) and (4.9), the left-hand side of (4.16) vanishes at leading order, which means that this term has the structure of a relaxation term in φ. The factor $\varphi^{(n-2)/2}$ on the left-hand side of (4.16) is introduced to avoid the appearance of a factor $(1/\lambda)^{(2-n)/n}$ in front of a source term further in the model, that would lead to a divergence in the case $\theta = 0$. The second term on the right-hand side of (4.16) also has a relaxation structure owing to (4.15). Finally, the integrated momentum (4.10) can thus be rewritten as

$$\frac{\partial}{\partial t}(hU) + \frac{\partial}{\partial x}\left(hU^2 + h^3\varphi + \frac{h^2}{2Fr^2}\right) = \\ \frac{1}{\varepsilon Re}\left[\lambda h[1-q(n,\xi)] - Bi - \alpha_1(n)\frac{U}{h}\left|\frac{U}{h}\right|^{n-1}\right]\beta_1(n,\xi,\zeta) \\ + \frac{\varphi^{\frac{n-2}{2}}}{\varepsilon Re}\left[\varphi - \alpha_2(n,\xi)\frac{U^2}{h^2}\right]\beta_2(n,\xi,\zeta), \tag{4.18}$$

where the functions β_1 and β_2 are given in Appendix B. The first relaxation term in (4.18) interprets as the balance between gravity, yield stress and viscous friction along the x-axis.

As will be shown later, writing the viscous friction term in the form of a power law in U/h is important to get proper free-surface shapes for steady-state surges (see § 6).

https://doi.org/10.1017/jfm.2026.11662 Published online by Cambridge University Press

The additional friction term $\lambda h\, q(n,\xi)$ is specific to the viscoplastic case (since $q=0$ if $\tau_c=0$) and originates from the consistency requirement when expressing the first source term as a sum of weight, yield stress and power-law viscous friction.

The second term on the right-hand side of (4.18) corresponds to a relaxation for the enstrophy. The terms with λhq and Bi in (4.18) formally oppose the flow and should, in general, depend on the sign of U. However, in the present study, we restrict our analysis to flow regimes with positive velocity values only.

4.3. *Enstrophy balance equation*

The mass and momentum (4.3) and (4.18) involve three unknown variables: h, U and φ. A third equation for an enstrophy balance is thus needed to close the problem. To that aim, we first consider the work–energy theorem (or kinetic energy equation), which in dimensional variables reads

$$\frac{\partial}{\partial t}\left(\frac{1}{2}\rho v^2\right)+\operatorname{div}\left(\frac{1}{2}\rho v^2\boldsymbol{v}\right)=\operatorname{div}(\boldsymbol{\sigma}\cdot\boldsymbol{v})-\boldsymbol{\sigma}:\frac{\dot{\boldsymbol{\gamma}}}{2}+\rho\boldsymbol{g}\boldsymbol{v}, \tag{4.19}$$

where $\boldsymbol{\sigma}=-p\boldsymbol{I}+\boldsymbol{\tau}$. Introducing the components of the vectors and tensors, we obtain the following expression in dimensionless form:

$$\begin{aligned}\frac{\partial}{\partial t}\left(\frac{u^2}{2}+\varepsilon^2\frac{w^2}{2}\right)+\frac{\partial}{\partial x}\left[u\left(\frac{u^2}{2}+\varepsilon^2\frac{w^2}{2}-\frac{x\tan\theta}{\varepsilon Fr^2}+\frac{z}{Fr^2}\right)+\frac{pu}{Fr^2}-\frac{Bi}{Re}(\tau_{xx}u+\varepsilon\tau_{xz}w)\right]\\ +\frac{\partial}{\partial z}\left[w\left(\frac{u^2}{2}+\varepsilon^2\frac{w^2}{2}-\frac{x\tan\theta}{\varepsilon Fr^2}+\frac{z}{Fr^2}\right)+\frac{pw}{Fr^2}-\frac{Bi}{\varepsilon Re}\tau_{xz}u-\frac{Bi}{Re}\tau_{zz}w\right]\\ =-\frac{2Bi}{Re}\left(\tau_{xx}^Y+2\frac{\varepsilon}{Bi}\frac{\partial u}{\partial x}\right)\frac{\partial u}{\partial x}-\frac{Bi}{\varepsilon Re}\left(\tau_{xz}^Y+\frac{1}{Bi}\left(\frac{\partial u}{\partial z}+\varepsilon^2\frac{\partial w}{\partial z}\right)\right)\left(\frac{\partial u}{\partial z}+\varepsilon^2\frac{\partial w}{\partial z}\right).\end{aligned} \tag{4.20}$$

This equation is averaged over the depth using the boundary conditions and neglecting all terms smaller than $O(\varepsilon\delta^{1/n-1})$. We omit this lengthy but algebraically straightforward derivation. The conservative left-hand side matches the classical structure formulated in Richard & Gavrilyuk (2012), whereas the right-hand side is given by relaxation terms similar to those introduced for the momentum (4.18). The final depth-averaged energy equation reads

$$\begin{aligned}\frac{\partial}{\partial t}\left(\frac{hU^2}{2}+\frac{h^3\varphi}{2}+\frac{h^2}{2Fr^2}\right)+\frac{\partial}{\partial x}\left(\frac{hU^3}{2}+\frac{3h^3U\varphi}{2}+\frac{h^2U}{Fr^2}\right)\\ =\frac{U}{\varepsilon Re}\left[\lambda h(1-q(n,\xi))-Bi-\alpha_1(n)\frac{U}{h}\left|\frac{U}{h}\right|^{n-1}\right]\Gamma_1(n,\xi,\zeta)\\ +\frac{U\varphi^{\frac{n-2}{2}}}{\varepsilon Re}\left[\varphi-\alpha_2(n,\xi)\frac{U^2}{h^2}\right]\Gamma_2(n,\xi,\zeta).\end{aligned} \tag{4.21}$$

Here the functions Γ_1 and Γ_2 are given in Appendix B. The first relaxation term on the right-hand side of (4.21) interprets as the balance between the power of weight, of yield stress and of viscous friction. The second term corresponds to the relaxation for the enstrophy φ.

https://doi.org/10.1017/jfm.2026.11662 Published online by Cambridge University Press

By combining (4.3), (4.18) and (4.21), an evolution equation for the enstrophy can be derived. This equation can be written as

$$\frac{h^2}{2}\left(\frac{\partial h\varphi}{\partial t}+\frac{\partial hU\varphi}{\partial x}\right)=\frac{U}{\varepsilon Re}\left[\lambda h(1-q(n,\xi))-Bi-\alpha_1(n)\frac{U}{h}\left|\frac{U}{h}\right|^{n-1}\right]r_1(n,\xi,\zeta)+\frac{U\varphi^{\frac{n-2}{2}}}{\varepsilon Re}\left[\varphi-\alpha_2(n,\xi)\frac{U^2}{h^2}\right]r_2(n,\xi,\zeta). \tag{4.22}$$

Here the functions r_1 and r_2 are given in Appendix B. It can be checked that $r_2(n,\xi,\zeta)<0$, indicating that the enstrophy relaxes properly towards its equilibrium value $\alpha_2(\xi,n)U^2/h^2$.

The system of conservation (4.3), (4.18), (4.21) and the system (4.3), (4.18), (4.22) are hyperbolic and create discontinuities – or shocks – in finite time. Apart from shocks, the two systems are equivalent. In the case of a shock, solving system (4.3), (4.18), (4.21) leads to conservation of energy and production of enstrophy. On the other hand, solving system (4.3), (4.18), (4.22) leads to conservation of enstrophy and dissipation of energy. A production of enstrophy at shocks is relevant in open-channel hydraulics to model the apparition of a turbulent roller in hydraulic jumps or turbulent roll waves with a mechanism similar to that of breaking waves (Richard & Gavrilyuk 2012, 2013; Richard 2024). Conversely, the enstrophy is conserved – and the energy is dissipated – when the enstrophy is due to bottom friction or viscous shearing (see Richard (2024) and Deleage & Richard (2025), for turbulent roll waves and granular flows, respectively). In the present case of a viscoplastic flow, enstrophy arises from viscous shearing associated with bottom friction, in the absence of turbulent rollers or wave-breaking mechanisms. Therefore, the enstrophy (4.22) is solved instead of the energy (4.21), along with the mass and momentum (4.3) and (4.18).

4.4. *Structure of the model for material stoppage*

An important requirement for viscoplastic flow models is the ability to describe the stoppage of the material. However, the structure of the system (4.3), (4.18) and (4.22) cannot account for this feature. Formally, the final shape of the material after stoppage should satisfy the condition $h\leqslant h_p$ for any x, since the opposite situation would immediately generate yielding due to the gravity term λh being larger than the plastic term Bi. However, the asymptotic expansions derived in § 3 are valid only for $h>h_p$. Hence, it cannot be guaranteed that the coefficients β_1, β_2, r_1 and r_2 remain well-behaved for $h\leqslant h_p$. This drawback comes from the fact that the thickness of the pseudoplug is supposed to be constant in the asymptotic expansions. As we show below, the coefficients can nevertheless be modified to properly capture stoppage, although this regime is formally outside of the validity of the asymptotic approach. To that aim we use the following strategy: let us first consider that $h\leqslant h_p$ and that the material is highly sheared. In this case, the material is expected to behave similarly to a power-law fluid, so that instead of the coefficients β_1, β_2, r_1 and r_2, we expect to recover their power-law limits:

$$\beta_1(0,0,n)=1, \tag{4.23}$$

$$r_1(0,0,n)=0, \tag{4.24}$$

$$\beta_2^*(n)=\beta_2(0,0,n)\equiv\frac{1}{2}n^{1-3n/2}(2n+1)^{n-1}(3n+2)^{n/2}(4n+3), \tag{4.25}$$

https://doi.org/10.1017/jfm.2026.11662 Published online by Cambridge University Press

$$r_2^*(n) = r_2(0,0,n) \equiv -\frac{1}{2} n^{1-3n/2}(n+1)(2n+1)^{n-2}(3n+2)^{n/2}(4n+3). \tag{4.26}$$

To ensure a consistent transition from the original coefficients β_1, β_2, r_1 and r_2 to their power-law limits (4.23)–(4.26) for $h \leqslant h_p$, let us introduce the following function:

$$f(n,\varphi,\xi) = \begin{cases} \exp\left(2 - \dfrac{\varphi}{\varphi^{(0)}(n,\xi)} - \dfrac{\varphi^{(0)}(n,\xi)}{\varphi}\right), & \text{for } \xi < 1 \text{ and } \varphi > 0, \\ 0, \quad \text{otherwise}, \end{cases} \tag{4.27}$$

where $\varphi^{(0)}$ is given by (4.9). An important property of f is that a multiplication of the source terms by this function does not change the order of consistency of the model, since $f(n,\varphi,\xi) = 1 + O(\varepsilon^2)$. This function can thus be used to cancel out unwanted terms when $h \leqslant h_p$. Taking into account this property, the momentum (4.18) and enstrophy balance (4.22) can be rewritten consistently as

$$\begin{aligned} &\frac{\partial}{\partial t}(hU) + \frac{\partial}{\partial x}\left(hU^2 + h^3\varphi + \frac{h^2}{2Fr^2}\right) = \\ &\quad + \frac{1}{\varepsilon Re}\left[\lambda h(1-q(n,\xi)) - Bi - \alpha_1(n)\frac{U}{h}\left|\frac{U}{h}\right|^{n-1}\right]\Big(1 + \big[\beta_1(n,\xi,\zeta) - 1\big] f(n,\varphi,\xi)\Big) \\ &\quad + \frac{\varphi^{\frac{n-2}{2}}}{\varepsilon Re}\left[\varphi - \alpha_1(n)\frac{U^2}{h^2}\right]\Big(\beta_2^*(n) + \big[\beta_2(n,\xi,\zeta) - \beta_2^*(n)\big] f(n,\varphi,\xi)\Big), \end{aligned} \tag{4.28}$$

$$\begin{aligned} &\frac{h^2}{2}\left(\frac{\partial h\varphi}{\partial t} + \frac{\partial hU\varphi}{\partial x}\right) = \\ &\quad \frac{U}{\varepsilon Re}\left[\lambda h(1-q(n,\xi)) - Bi - \alpha_1(n)\frac{U}{h}\left|\frac{U}{h}\right|^{n-1}\right] r_1(\xi,n,\zeta) f(n,\varphi,\xi) \\ &\quad + \frac{U\varphi^{\frac{n-2}{2}}}{\varepsilon Re}\left[\varphi - \alpha_1(n,\xi)\frac{U^2}{h^2}\right]\Big(r_2^*(n) + \big[r_2(n,\xi,\zeta) - r_2^*(n)\big] f(n,\varphi,\xi)\Big). \end{aligned} \tag{4.29}$$

It should be noted that the function $q(n,\xi)$ is also not well-defined for $\xi < 1$ ($h < h_p$). Hence, we consider its limiting value $q(n,1) = 0$ for any $\xi \leqslant 1$.

If now $h \leqslant h_p$ and the material is only slightly sheared, the fluid is expected to slow down and progressively stop. In this case, the fluid velocity and enstrophy are small, such that the dominant terms in (4.28) and (4.29) are the hydrostatic pressure, the gravity and the yield stress. In particular, when the material is stopped ($U = 0$, $\varphi = 0$ and $h \leqslant h_p$), the momentum balance (4.28) properly reduces to

$$\lambda h\left(1 - \varepsilon \cot\theta \frac{\partial h}{\partial x}\right) = Bi, \tag{4.30}$$

which is the classical equation for a static surge stopped on an inclined plane, as used in several previous studies (Balmforth *et al.* 2006; Hogg & Matson 2009; Dubash *et al.* 2009). Note also that both the left- and right-hand sides of the enstrophy (4.29) are zero when the fluid is stopped. This is not the case for the original (4.22): here the first source term is never zero (except if $h = h_p$), which would prevent equality between the left- and right-hand sides at stoppage. Hence, the consistent modification of the source term coefficients in (4.28) and (4.29) properly captures the expected flow behaviour for $h \leqslant h_p$ both when the fluid is highly and slightly sheared: in the former case the fluid behaves as a power-law fluid, while in the latter case the material converges to a stoppage.

https://doi.org/10.1017/jfm.2026.11662 Published online by Cambridge University Press

Lastly, note that (4.30) only refers to the relation between driving and resisting forces after stoppage. In general, the full stoppage criterion reads

$$\left|\lambda h\left(1-\varepsilon\cot\theta\frac{\partial h}{\partial x}\right)-\varepsilon Re\left[\frac{\partial}{\partial t}\left(hU\right)+\frac{\partial}{\partial x}\left(hU^2+h^3\varphi\right)\right]\right|\leqslant Bi\ \ \Rightarrow\ \ (U,\varphi)=0, \tag{4.31}$$

meaning that the material moves only when the sum of the driving forces (weight, pressure gradient and inertia) overcomes the yield stress. Furthermore, (4.30) describes only one of the possible equilibrium shapes of the viscoplastic material at stoppage. This scenario happens when the fluid velocity decreases to zero as the driving forces approach the balance with the yield stress. In a more general case, it is also possible to have situations for which the fluid velocity is still large, while the sum of the gravity and hydrostatic pressure has already become smaller than the yield stress. In this case, according to the momentum (4.28), the source terms will become largely negative, slowing down the fluid and leading to an abrupt stoppage. Therefore, a more general condition at stoppage is

$$\lambda h\left(1-\varepsilon\cot\theta\frac{\partial h}{\partial x}\right)\leqslant Bi. \tag{4.32}$$

This issue is further elaborated in § 5.3.2, where we simulate dam-break surges and study different shapes after stoppage.

4.5. *The model in dimensional variables*

In dimensional variables, the system of (4.3), (4.28) and (4.29) is rewritten as

$$\frac{\partial h}{\partial t}+\frac{\partial hU}{\partial x}=0, \tag{4.33}$$

$$\begin{aligned}\frac{\partial}{\partial t}\left(hU\right)+\frac{\partial}{\partial x}\left(hU^2+h^3\varphi\right)&=-\frac{\partial}{\partial x}\frac{gh^2\cos\theta}{2}\\&+\left[gh\sin\theta(1-q(n,\xi))-\frac{\tau_c}{\rho}-\alpha_1(n)\nu\frac{U}{h}\left|\frac{U}{h}\right|^{n-1}\right]\Big(1+\big[\beta_1(n,\xi,\zeta)-1\big]f(n,\varphi,\xi)\Big)\\&+\varphi^{\frac{n-2}{2}}\left[\varphi-\alpha_2(n,\xi)\frac{U^2}{h^2}\right]\Big(\beta_2^*(n)+\big[\beta_2(n,\xi,\zeta)-\beta_2^*(n)\big]f(n,\varphi,\xi)\Big),\end{aligned} \tag{4.34}$$

$$\begin{aligned}\frac{h^2}{2}\left(\frac{\partial h\varphi}{\partial t}+\frac{\partial hU\varphi}{\partial x}\right)&=\\U\left[gh\sin\theta(1-q(n,\xi))-\frac{\tau_c}{\rho}-\alpha_1(n)\nu\frac{U}{h}\left|\frac{U}{h}\right|^{n-1}\right]&r_1(n,\xi,\zeta)f(n,\varphi,\xi)\\+U\varphi^{\frac{n-2}{2}}\left[\varphi-\alpha_2(n,\xi)\frac{U^2}{h^2}\right]&\Big(r_2^*(n)+\big[r_2(n,\xi,\zeta)-r_2^*(n)\big]f(n,\varphi,\xi)\Big),\end{aligned} \tag{4.35}$$

where $\nu=K/\rho$, $\xi=\tau_c/(\rho gh\sin\theta)$ and $\zeta=\delta/h$. The functions α_i $(i=1,2)$ and q are defined in § 4.2. The functions r_i and β_i $(i=1,2)$ are defined in Appendix B. The functions β_2^*, r_2^* and f are defined in § 4.4. Note that the parameter of pseudoplug shearing δ is here dimensional and can be interpreted as the thickness of the thin intermediate layer located between the sheared layer and the pseudoplug, in which the 'Bingham plateau' regularization contributes to the first-order correction of the velocity asymptotic expansion (A11). For completeness, the stoppage criterion (4.31) in

https://doi.org/10.1017/jfm.2026.11662 Published online by Cambridge University Press

dimensional variables reads

$$\left| gh\sin\theta - \frac{\partial}{\partial x}\frac{gh^2\cos\theta}{2} - \frac{\partial}{\partial t}(hU) - \frac{\partial}{\partial x}\left(hU^2 + h^3\varphi\right)\right| \leqslant \frac{\tau_c}{\rho} \;\Rightarrow\; (U,\varphi) = 0. \quad (4.36)$$

The left-hand side of the system (4.33)–(4.35) has the structure of the Euler equations for compressible fluids with $h^3\varphi$ and φ playing the roles of pressure and entropy, respectively. The model is therefore fully hyperbolic, enabling the implementation of an efficient well-balanced numerical scheme, described in detail in Appendix C. The well-balanced property, i.e. the ability of the scheme to capture non-trivial static solutions satisfying the inequality (4.32), is ensured by treating the hydrostatic pressure as a source term and by employing a discretized stoppage criterion (C11). Importantly, although the final model is highly nonlinear and complex, it can still be regarded as computationally efficient. The first step of the numerical scheme, which involves solving the homogeneous system, is handled using the standard Rusanov Riemann solvers developed for classical systems of gas dynamics (e.g. see Toro 1999). This step is therefore straightforward and computationally inexpensive. The second step, which involves integrating the source terms, may appear more computationally demanding due to the length and complexity of the source-term expressions. Nevertheless, the use of a semi-implicit scheme allows the resulting algebraic system to be solved analytically with respect to the flow variables, thereby keeping the computational cost relatively low.

We recall that the model (4.33)–(4.35) is applicable only for $n < 1$ due to the specific regularization of the viscous stress tensor at $O(\varepsilon)$, except in the case $\delta = 0$, which corresponds to the model with zero shearing in the pseudoplug and is valid for any value of n. Although it is possible to adapt the regularization for $n > 1$, the existing real viscoplastic fluids are generally characterized by $n < 1$, and therefore we restricted our analysis to this case.

For the particular case of Bingham fluids ($n = 1$), the model is presented in Appendix D. This model is derived similarly to the model described above for Herschel–Bulkley fluids, but using the analytical asymptotic expansions obtained in Denisenko *et al.* (2023) (without the regularization parameter δ). Note that the model for Bingham fluids (D1)–(D3) cannot be obtained from the model (4.33)–(4.35) as $n \to 1$. This issue is due to the divergence of the effective viscosity for $n < 1$, that immediately leads to zero shearing in the pseudoplug for the asymptotic expansion at $O(\varepsilon)$. The introduction of the 'Bingham plateau' regularization with the parameter δ, which is introduced to recover non-zero shearing in the pseudoplug for $n < 1$, also slightly alters the expansion in the sheared layer ($z < h - h_p$) at $O(\varepsilon)$ for any values of n. Hence, at $n = 1$, the first-order correction (A11)–(A17) differs from that in Denisenko *et al.* (2023) for any values of δ.

Note also that the model for Bingham fluids presented in Appendix D differs from the model previously derived in Denisenko *et al.* (2023), since the latter was not adapted to describe flow stoppage. In particular, this new model includes the following modifications: the new definition of the enstrophy (4.7), which eliminates the need for the enstrophy to relax towards zero at $h = h_p$; the inclusion of the extra yield-stress friction term q, allowing the removal of the dependence of the viscous friction on the yield stress and avoiding the divergence at $h = h_p$; the adaptation of the coefficients in front of the source terms to ensure proper behaviour for $h \leqslant h_p$ and to correctly capture stoppage; the use of the enstrophy balance equation instead of the energy balance equation in order to conserve the enstrophy variable associated with the viscous shearing (Richard 2024).

For the case of power-law fluids (i.e. without yield stress), the model derived as a particular case of (4.33)–(4.35) with $\tau_c = 0$ and $\delta = 0$ is presented in Appendix E.

https://doi.org/10.1017/jfm.2026.11662 Published online by Cambridge University Press

Note that this model is applicable for any value of n, since no regularization is required in this case. To the best of our knowledge, this is the first time that the three-equation approach has been applied to the power-law rheology.

5. Applications

5.1. *Long-wave instability*

Steady and uniform equilibrium flows down an inclined plane are unstable in a specific range of the flow parameters. Balmforth & Liu (2004) studied the linear stability of the equilibrium flow based on the linearized Cauchy equations (or generalized Orr–Sommerfeld equations) in the case of a Herschel–Bulkley fluid with zero shearing in the pseudoplug. In order to compare our results with this study, we use here the same characteristic velocity, namely $u_0 = (\rho g h_0^{1+n} \sin\theta/K)^{1/n}$. Note that this choice leads to $\lambda = 1$.

The system of (4.3), (4.28) and (4.29) is linearized around the leading-order solution (4.2) and (4.9). Let us consider $h = 1 + h'$, $U = U^{(0)} + U'$ and $\varphi = \varphi^{(0)} + \varphi'$ with small sinusoidal perturbations: $[h', U', \varphi'] = [A_1, A_2, A_3]\exp[\mathrm{i}k(x - ct)]$. The parameter k is the wavenumber and c is the phase velocity. The dispersion relation is derived by equating the determinant of the linearized system to zero, which yields

$$c = \lambda^{\frac{1}{n}}(1 - h_p)^{\frac{1}{n}} + \mathrm{i}\varepsilon k\, c_1(Re, n, h_p, \delta) + O(\varepsilon^2). \tag{5.1}$$

The expression of the first-order correction to the phase velocity c_1 is lengthy and does not need to be provided here. In the long-wave limit (large k), the base flow is stable if $c_1 < 0$. This leads to stability criterion $Re < Re_c$, with the critical Reynolds number Re_c given by

$$Re_c = \frac{\cot\theta(n+1)(n+2)(3n+1)(3n+2)(4n+1)}{(1-Bi)^{\frac{2}{n}} D(n, Bi, \delta)}\Big[\delta^{1/n-1}(n+1)(2n+1) + 3n\big(2nBi(nBi+1)+n+1\big)(1-Bi)^{\frac{1}{n}}\Big], \tag{5.2}$$

where

$$\begin{aligned} D(n, Bi, \delta) = {} & 3n(3n+1)(4n+1)\,(1-Bi)^{\frac{1}{n}}\big(nBi\big(n(n(6n+19)+11)Bi\,(nBi+2) \\ & - \delta^{1/n-1}(n+1)(n+2)(3n+2)\big(nBi\big(3nBi\big(4n^2\big(Bi^2-3\big)+n(4Bi-5)+1\big) \\ & - n(32n+15) - 1\big) + (n+2)(9n+7)\big) + 2(n+2)(n+1)^2\big) - (n+1)(3n+1)(5n+1)\big). \end{aligned} \tag{5.3}$$

Due to the term $(1 - Bi)^{\frac{2}{n}}$ in the denominator of (5.2), the critical Reynolds number Re_c increases as the Bingham number increases. This corresponds to a stabilizing effect of the plasticity, which was also obtained in former studies (Balmforth & Liu 2004; Denisenko *et al.* 2023). Note that a different result would be obtained by implementing the non-zero shearing in the pseudoplug through asymptotic expansions built in the framework of the classical tensorial extension of the constitutive law. In this case, a destabilizing effect of plasticity is observed at large slope angles (see Denisenko *et al.* (2023) for Bingham fluids), leading to an implausible prediction of absolutely unstable rigid solid under small perturbations. Although there are no experimental reports of instability of viscoplastic fluids at large slope angles, the existing results for smaller angles consistently show a stabilizing effect of plasticity (e.g. Noma *et al.* 2021).

https://doi.org/10.1017/jfm.2026.11662 Published online by Cambridge University Press

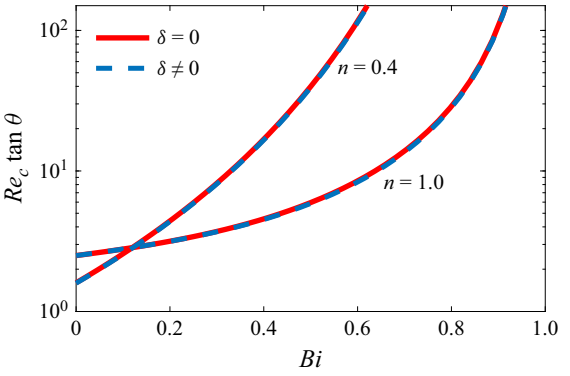


Figure 2. Instability thresholds predicted by the three-equation model: critical Reynolds number $Re_c \tan\theta$ as a function of the Bingham number Bi. For $n = 0.4$, the red and blue curves correspond to the threshold (5.2) with $\delta = 0$ and $\delta = 0.2$, respectively. For $n = 1$, the red curve corresponds to (5.2) with $\delta = 0$, while the blue curve corresponds to the threshold (D9) obtained for the Bingham fluid model (D1)–(D3).

In the case $\delta = 0$, i.e. for zero shearing in the pseudoplug, (5.2) reduces to

$$Re_c = \frac{\cot\theta\,(n+1)(n+2)(3n+2)\,(1-Bi)^{-2/n}\,(2nBi\,(nBi+1)+n+1)}{nBi\,(n(n(6n+19)+11)Bi\,(nBi+2)+(n+2)(9n+7))+2(n+2)(n+1)^2}, \tag{5.4}$$

which exactly coincides with the expression obtained by Balmforth & Liu (2004). This result is made possible by the consistency of our three-equation model and the fact that for $\delta = 0$ the velocity expansion (A11)–(A17) is the same as that used by Balmforth & Liu (2004).

Figure 2 presents the evolution of the critical Reynolds number Re_c as a function of Bi for different values of n and δ. For power-law fluid ($Bi = 0$), Re_c decreases as n decreases. An opposite trend is observed for viscoplastic fluids if the Bingham number is large enough: in this case a decrease in the power-law index n leads to stabilization of the flow. This effect was already highlighted in Balmforth & Liu (2004). Conversely, variations in δ produce hardly visible differences: the curves corresponding to $\delta = 0$ and to $\delta = 0.2$ are almost identical. Hence, the influence of a slight shearing of the pseudoplug on the stability criterion is small. In detail, the curves for $\delta = 0.2$ are slightly below those for $\delta = 0$, showing a slight destabilizing effect of the shearing in the pseudoplug. This finding supports the intuitive expectation that shearing in the pseudoplug, by suppressing fluid rigidity, makes the flow more prone to instability.

Based on comparisons with experimental data, Noma *et al.* (2021) showed that (5.4) predicts relatively well the instability thresholds for the real viscoplastic fluids. As shown in figure 3, our criterion (5.2) yields the same agreement with experiments, irrespective of whether δ is zero or non-zero.

5.2. *Simulation of roll waves*

We study here the development of roll waves from equilibrium flows under small perturbations. Such waves correspond to flow regimes that remain relatively close to equilibrium and therefore lie within the validity domain of the assumptions underlying the model derivation. An initially uniform flow satisfying the leading-order solution (4.2) and (4.9) is perturbed by applying a small sinusoidal disturbance of fixed frequency at the entrance of the system. The length of the computational domain is $L = 3.0$ m, the mesh size is $\mathrm{d}x = 0.5$ mm and Courant–Friedrichs–Lewy number is 0.5. The depth of the

https://doi.org/10.1017/jfm.2026.11662 Published online by Cambridge University Press

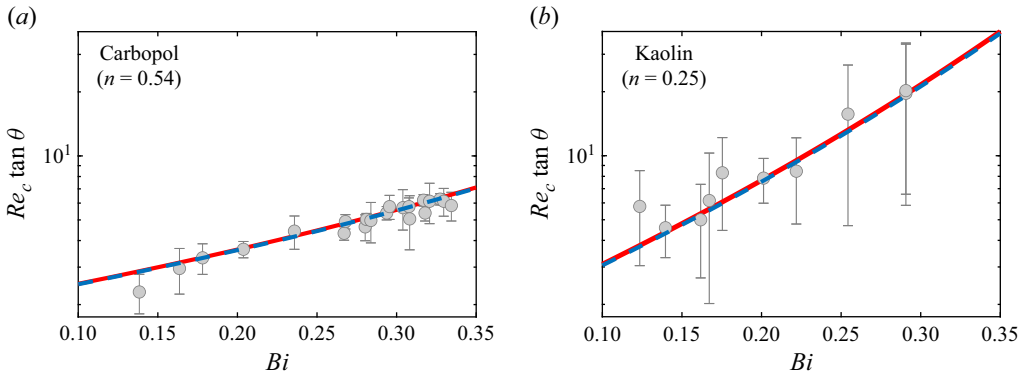


Figure 3. Instability thresholds obtained from our model with $\delta = 0$ (red curve) and with $\delta = 0.2$ (blue curve) compared with the experimental results of Noma *et al.* (2021) (grey dots) for Carbopol (*a*) and kaolin (*b*).

uniform flow is $h_0 = 10$ mm and the angle of the slope is $\theta = 20°$. At the entrance, the flow height h is perturbed at a frequency of 2.0 Hz, the discharge hU is preserved and the enstrophy φ is taken equal to $\varphi^{(0)}(h)$ with the perturbed value of h. At the outlet, a Neumann boundary condition is considered. We explore the influence of the shear-thinning and the plasticity on the simulated roll waves by varying the values of n and Bi. Additionally, we explore the influence of the shearing in the pseudoplug by varying the parameter δ. The values of Reynolds and Froude numbers are fixed for all simulations ($Re = 37.28$ and $Fr = 3.68$), in order to isolate the influence of variations in the other parameters.

Figure 4 shows the simulated roll waves for all parameter cases in dimensional form. It is clearly observed that an increase of plasticity, i.e. of the Bingham number, leads to a decrease of the roll wave amplitude and wavelength. This result has already been highlighted by Denisenko *et al.* (2023) and can be related to the stabilizing effect of plasticity. The influence of shear-thinning, i.e. of the power-law index n, is less straightforward. For $Bi = 0.35$, a decrease in n leads to a decrease of the roll wave amplitude and their wavelength. For $Bi = 0.05$, a decrease in n leads to an increase of the roll wave amplitude and to a decrease of their wavelength. These different effects can be related to the evolution of the instability criterion and the crossover observed for $Bi \approx 0.1$ in figure 2: in general, the larger the distance $Re - Re_c$ between the fixed Reynolds number and the critical value, the larger the wave amplitude. Generally, however, this rule seems to be valid only in the vicinity of the critical values of the Reynolds number.

Figure 4 also illustrates the influence of shearing in the pseudoplug. Recall that, for $n = 1$ (Bingham fluid), the model with non-zero shearing in the pseudoplug is derived without any parameter δ (see Appendix D), while, for $n \neq 1$, the model with zero shearing in the pseudoplug is derived from the general model (4.33)–(4.35) with $\delta = 0$. Although the difference $Re - Re_c$ slightly increases as δ increases (see figure 2), an increase in δ generally leads to a slight decrease in the roll wave amplitudes, for both values of n. This behaviour is presumably due to the fact that shearing in the pseudoplug layer introduces an extra energy dissipation, which slightly damps the growth of the roll waves.

Fiorot *et al.* (2024) recently reported on experimental roll waves generated with a viscoplastic fluid. Figure 5 shows a comparison between these experimental results and the prediction of the three-equation model. For this simulation, we use the same parameters as in the experiments: $n = 0.39$, $\theta = 20°$, $\rho = 1003.2$ kg m^{-3}, $\tau_c = 9.56$ Pa, $K = 5.73$ Pa s^n and $h_0 = 12.56$ mm. The length of the channel is 2.5 m, and the frequency applied at the inlet is 1.5 Hz.

https://doi.org/10.1017/jfm.2026.11662 Published online by Cambridge University Press

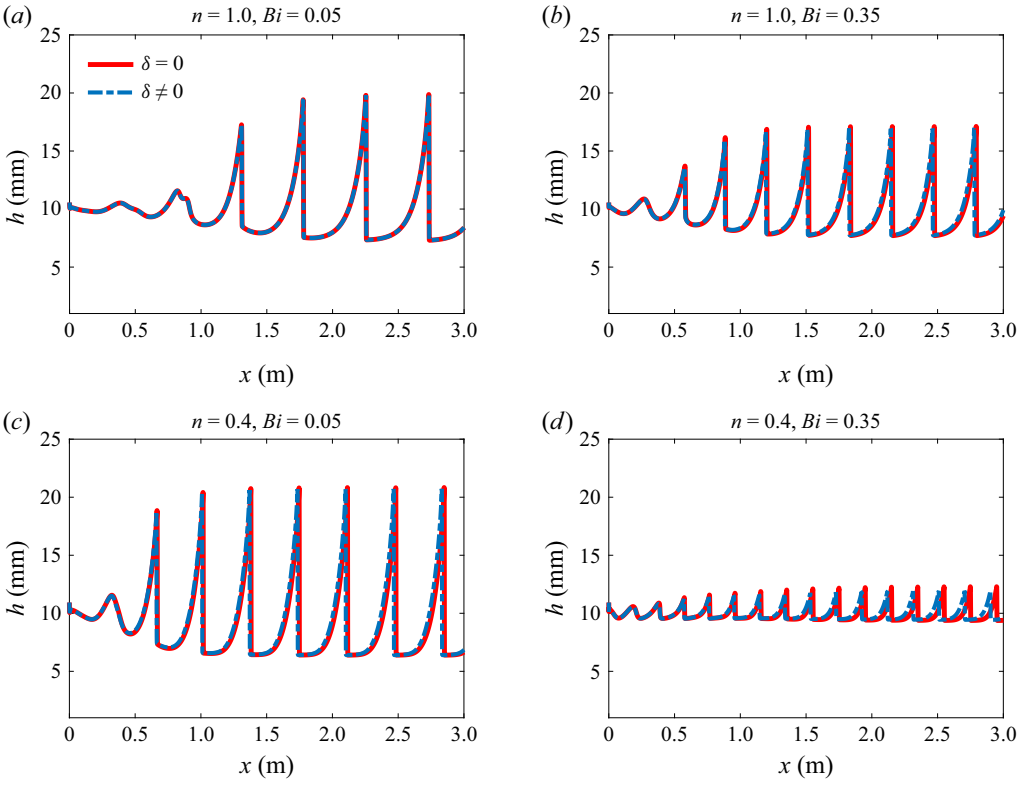


Figure 4. Numerical simulations of roll waves with the three-equation model: evolution of flow depth h as a function of distance from inlet x for different values of n and Bi. For $n = 0.4$, the red and blue curves are obtained from (4.33)–(4.35) with $\delta = 0$ and $\delta = 0.2$, respectively. For $n = 1$, the red curve is computed from (4.33)–(4.35) with $\delta = 0$, while the blue curve is computed from the Bingham fluid model (D1)–(D3). Other parameters are $Re = 37.28$, $Fr = 3.68$, $\lambda = 1$ and $\theta = 20°$.

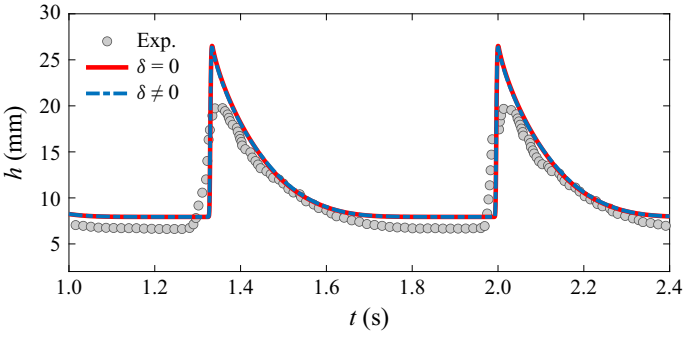


Figure 5. Comparison between simulated roll waves and the experimental results of Fiorot *et al.* (2024): variation of the depth h at a function of time at $x = 1.5$ from the disturbance – grey dots corresponds to the experimental data Fiorot *et al.* (2024), blue and red curves correspond to numerical results with $\delta = 0$ and $\delta = 0.2$, respectively. Other parameters are indicated in the text.

It is observed that the agreement with the experiments is relatively good behind the wavefronts. However, the amplitude of the waves in the simulation is notably larger than in the experiments. This discrepancy is presumably related to the fact that the model at $O(\varepsilon)$ does not include any diffusion effect, such that the simulated roll waves are in fact shock

https://doi.org/10.1017/jfm.2026.11662 Published online by Cambridge University Press

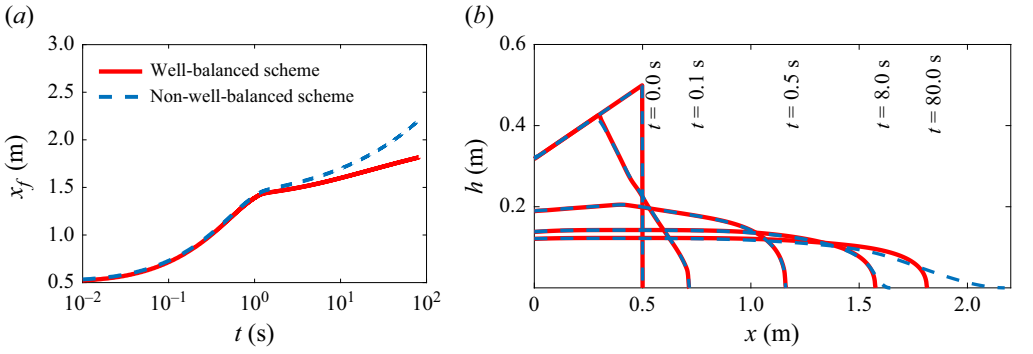


Figure 6. Simulation of a viscoplastic dam-break: front position x_f as a function of time (a) and flow depth profiles at different times (b). Red curves, numerical scheme with hydrostatic pressure taken as a source term; blue curves, numerical scheme with hydrostatic pressure taken as the part of the momentum flux. Parameters of the flow are $\tau_c = 350$ Pa, $K = 200$ Pa s^n, $n = 0.4$, $\rho = 1000$ kg m^{-3}, $\theta = 20°$ and $\delta = 0$.

waves. Diffusion effects, proportional to second-order derivatives, would smooth out these shocks and lead to a decrease in wave amplitude. In practice, considering such effects in a consistent manner would require the derivation of higher-order terms by continuing the asymptotic expansions up to $O(\varepsilon^2)$. Note also that, in this case, the shearing in the pseudoplug zone (parameter δ) has essentially no effect on the free-surface shape.

5.3. *Dam-break simulations*

We consider here the classical dam-break problem for a viscoplastic material. In this case, due to the existence of a dry front and to the possibility of a flow stoppage, the flow is far from the equilibrium flow and therefore lies outside the assumptions underlying the model derivation. This case can thus be used to assess the validity of the strategy presented in § 4.4.

An initial volume of material is filled into a rectangular box of length l, which is located upstream of the inclined plane. The rear end of this reservoir is chosen as the origin of the coordinate system. The box is equipped with a gate perpendicular to the slope, which is suddenly opened at $t = 0$. The initial flow depth is thus given by

$$h_0(x) = \begin{cases} h_g + (x - l)\tan\theta, & 0 \leqslant x \leqslant l, \\ 0, & l \leqslant x, \end{cases} \tag{5.5}$$

with h_g the fluid height at the gate.

The typical dynamics of the flow is presented in figure 6. Two different numerical solutions of the three-equation model are compared, which differ by treating the hydrostatic pressure as a source term (red curve) or as a part of the momentum flux (blue line) (see Appendix C.5). Two main flow regimes separated by a relatively abrupt transition are observed. At early times, an inertially dominated regime lasts for approximately 1 s and is characterized by a rapid propagation of the front. The front then slows down in the second regime, which corresponds to a balance between gravity, yield stress, viscous friction and hydrostatic pressure. The two numerical schemes provide similar results for the first regime, both in terms of front velocity and free-surface shape. In particular, they reproduce a contact angle close to 90° at the front, as expected for such viscous fluids. In the second regime, however, the non-well-balanced numerical scheme with the pressure in the flux tends to overestimate the front speed and loses the 90° contact angle. This 'smearing' of the front is due to the fact that, with this scheme, the numerical

https://doi.org/10.1017/jfm.2026.11662 Published online by Cambridge University Press

diffusion becomes dominant in the mass equation at small velocities (for more details see Appendix C.5). In contrast, the well-balanced numerical scheme with the pressure in the source terms preserves a realistic front shape as the flow progressively slows down.

Similar differences between well-balanced and not well-balanced schemes were already highlighted by Fernández-Nieto *et al.* (2023), who used another well-balanced scheme based on hydrostatic reconstruction of the depth variable. However, the authors reported that their scheme becomes mesh-dependent in the slowly creeping regime, leading to an overestimation of the front velocity. In contrast, the scheme proposed in the present work does not show such a drawback.

5.3.1. *Comparison with experiments*

To evaluate the predictions of the model, we simulate the experiments reported by Ancey & Cochard (2009). These authors used a Carbopol material characterized by the following parameters: $\tau_c = 32.1$ Pa, $K = 78$ Pa s^n, $n = 0.388$ and $\rho = 1000$ kg m^3. The length of the reservoir is $l = 0.51$ m and four values of slope angle are considered: $\theta = 6°;\ 12°;\ 18°;\ 24°$. For these slopes, the gate aperture h_g is 0.26 m, 0.23 m, 0.20 m and 0.177 m, respectively. For the numerical simulations, we use the consistent three-equation model (4.33)–(4.35) with $\delta = 0$. We checked that varying the parameter δ (shearing in the pseudoplug) has essentially no influence in this case. To illustrate the influence of inertia, we also plot the results of the inertialess lubrication model presented by Ancey & Cochard (2009).

Figure 7 compares the evolution of front position for the two models and the experiments. The experimental results exhibit two main regimes separated by a relatively abrupt transition. At early times, an inertially dominated regime persists for approximately one second and is characterized by rapid front propagation. Next, the flow enters a second, slow creeping regime characterized by a deceleration of the front. It is observed that the lubrication model, which does not include inertial terms, cannot capture the first regime. In the second regime, the lubrication model predicts a trend parallel to the experimental data but with a slight shift. In contrast, the three-equation model captures the first regime and the transition relatively well. In the second regime, the three-equation model coincides almost exactly with the lubrication model, as expected, and the slight shift with the experimental data is again observed. This shift may relate to the sidewall friction, as suggested by Andreini, Epely-Chauvin & Ancey (2012). These authors pointed out that similar shifts appear in the modelling of dam-break problems for Newtonian fluids and can be eliminated by incorporating a sidewall friction term into the model. However, to the best of our knowledge, there is no general method for modelling sidewall friction in open-channel flows of viscoplastic fluids (e.g. Coussot 1994).

Another discrepancy with the experiments is observed at long times for the smaller angles ($\theta = 12°$ and $6°$). In the predictions of both the lubrication and the three-equation model, the yield stress term becomes dominant, so that the material progressively approaches full stoppage. In the experiment, however, the material keeps moving without any noticeable slowdown. These deviations at long times could be due to some residual slip of the Carbopol on the bottom plane, such that the no-slip boundary condition (2.20) may not be completely valid in the experimental flows. A simple Navier-slip condition could potentially be incorporated into the model within the framework of the considered constitutive law, although this would lead to lengthy algebraic modifications in the asymptotic expansion.

Flow depth profiles predicted by the three-equation model are compared with experiments in figure 8. A satisfactory agreement is found despite the differences in

https://doi.org/10.1017/jfm.2026.11662 Published online by Cambridge University Press

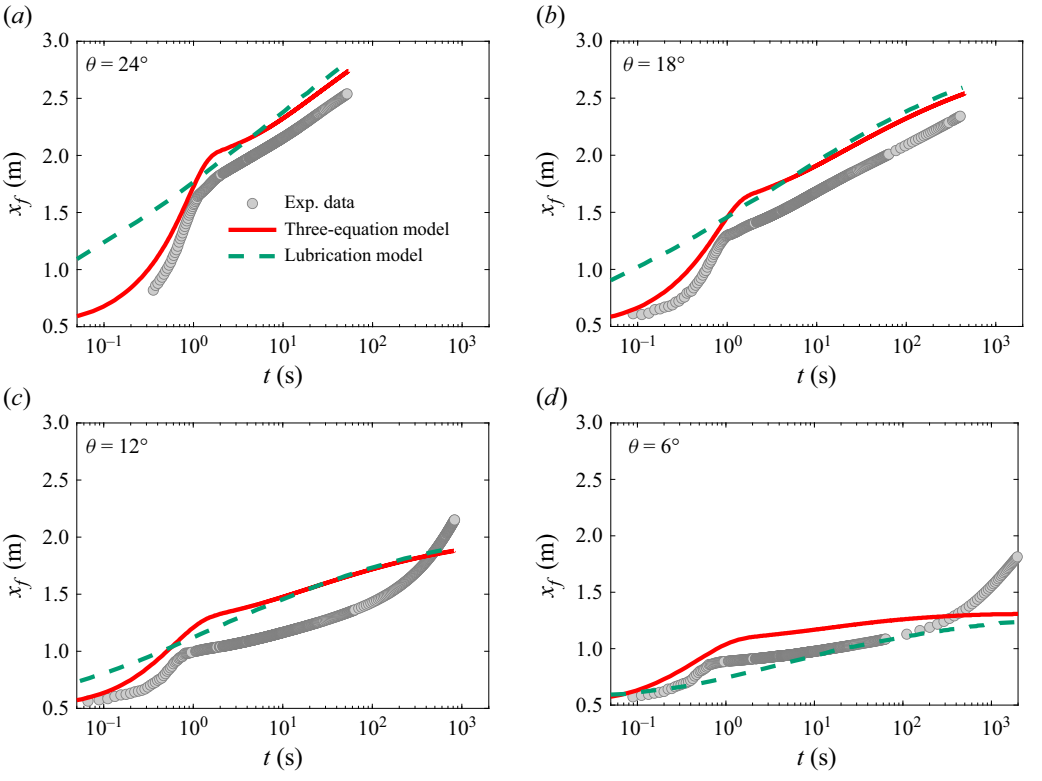


Figure 7. Comparison between dam-break simulations and experiments: front position x_f as a function of time for different slope angles. Experimental data and results of the lubrication model come from Ancey & Cochard (2009). The three-equation model (4.33)–(4.35) is simulated with $\delta = 0.0$.

front position. The fact that the maximum flow depth is not observed at the front in the experimental data at $t = 1.0$ s (for $\theta = 24°$ and $\theta = 18°$) is likely a consequence of the finite opening time of the gate.

Overall, the new three-equation shallow-flow model appears to capture relatively well the main trends observed in the experiments. Only few previous studies attempted such comparisons between shallow-flow models and experiments for viscoplastic dam breaks. Ancey *et al.* (2012) considered an inconsistent shallow-flow model and captured the inertia-dominated regime. However, they got an even larger shift with the experiments in the second regime, probably because these experiments were performed in a narrower channel. Later, comparisons with the same experiments were carried out by Fernández-Nieto *et al.* (2023), who used a multilayer shallow-flow model. Their result slightly improves the agreement with the data, in particular due to using a well-balanced scheme based on hydrostatic reconstruction. However, in both these studies, the predictions of the shallow-flow models deviate from those of the lubrication model at large times. Such deviations can be attributed to the numerical diffusion of the employed schemes and are similar to the behaviour observed with our model when the hydrostatic pressure is kept in the flux (see figure 6). Recently, Muchiri *et al.* (2024) proposed a new inconsistent shallow-flow model and reported good agreement with several experiments of Ancey & Cochard (2009). However, only large slope angles were considered. Additional comparisons at smaller slope angles would be useful. Furthermore, this model cannot describe stoppage of the material.

https://doi.org/10.1017/jfm.2026.11662 Published online by Cambridge University Press

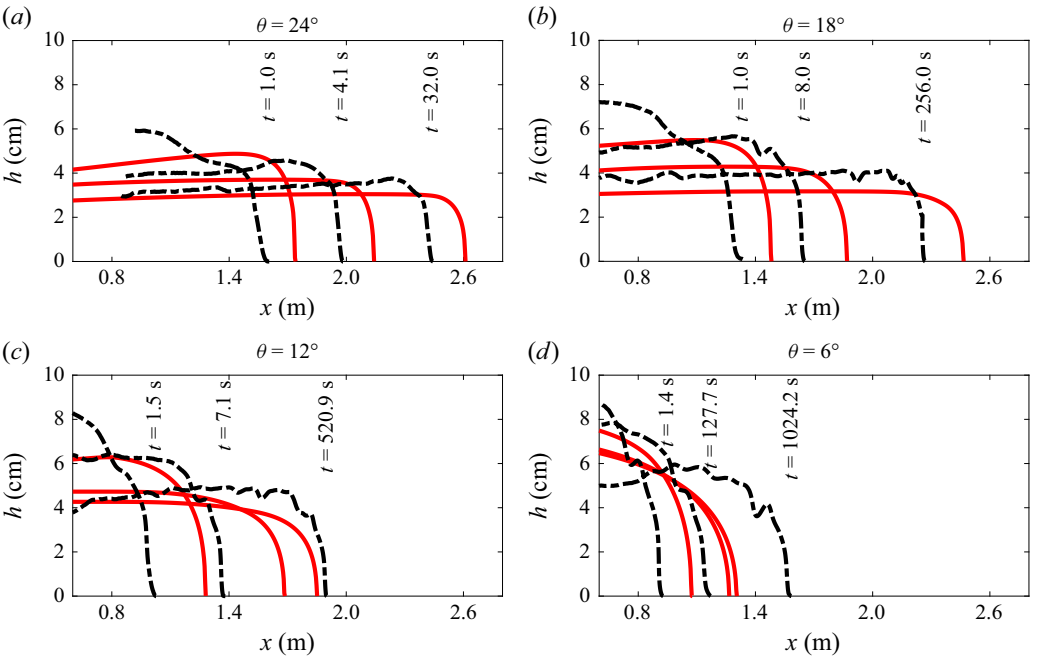


Figure 8. Comparison between dam-break simulations and experiments: flow-depth profiles for different slope angles. The red curve corresponds to the three-equation model (4.33)–(4.35); the black dashed line corresponds to the experimental data of Ancey & Cochard (2009).

5.3.2. *Flow stoppage*

We focus here on the long-time dynamics and final shape of the dam-break flow. Again, let us recall that the essential ingredient to properly capture full stoppage in our simulations is to consider the hydrostatic pressure as a source term in the numerical scheme (see Appendix C.5 for more details). As discussed in § 4.4, the final shape of the deposits should satisfy inequality (4.32) on the balance between hydrostatic pressure, gravity force and yield stress. In case of equality, (4.32) yields the ordinary differential (4.30) that was considered in several previous studies (Balmforth *et al.* 2006; Hogg & Matson 2009) to describes static surges stopped on an inclined plane. The free-surface shape predicted by this equation was shown to be in good agreement with experimental deposits of kaolin fluids (Coussot 1994). However, as was shown by Balmforth *et al.* (2006), deposit shapes do not systematically correspond to solutions of (4.30). Below we illustrate such phenomena in the framework of the three-equation model as well.

Figures 9 and 10 present the results of two dam-break simulations characterized by different rheological parameters, including the final stoppage. In figure 9(*a*), it is observed that the material slowly reaches a final shape satisfying (4.30). In the dynamics of the surge front (figure 9*b*), the two regimes already described can be distinguished, namely the inertially dominated regime ($0 \lesssim t \lesssim 10^0$ s) and the lubrication regime ($10^0 \lesssim t \lesssim 10^2$ s). A plasticity-dominated regime ($10^2 \lesssim t \lesssim 10^9$ s) then takes over at long times and slowly leads to stoppage, which is not reached before $t \gtrsim 10^8$ s in this case. These different regimes are also visible in the evolution of the velocity maximum (figure 9*c*). Note that at long times, the velocity maximum also demonstrates marked fluctuations. These fluctuations are associated with stop-and-go motions of the front. Typically, the front stops, while rear parts of the surge continue to move, causing a accumulation of material behind

https://doi.org/10.1017/jfm.2026.11662 Published online by Cambridge University Press

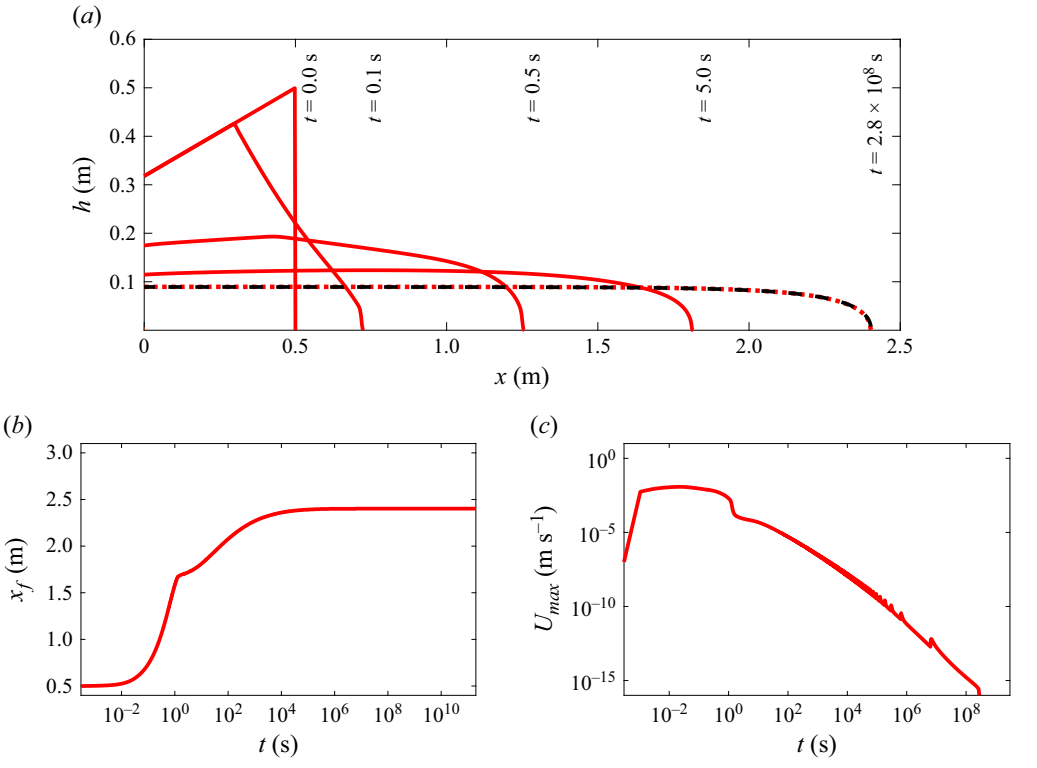


Figure 9. Dam-break simulation and final stoppage. (*a*) Flow depth profiles at different times: red solid curves are the numerical solutions of model (4.33)–(4.35); red dotted curve is the final shape at stoppage; black dashed line is the solution of (4.30) for the given volume. (*b*) Front position x_f as a function of time. (*c*) Velocity maximum U_{max} within the flow as a function of time. Parameters are $\tau_c = 300$ Pa, $K = 150$ Pa s^n, $n = 0.4$, $\theta = 20°$ and $\rho = 1000$ kg m^{-3}.

the front. This leads to a progressive increase of the pressure gradient until the yielding threshold is reached, resulting in a new displacement of the front.

In figure 10 the dynamics of the flow is markedly different. The material propagates quickly at the beginning but then suddenly stops. In this case, the shape after stoppage does not satisfy (4.30). This behaviour is due to the small value of consistency K but relatively large value of yield stress τ_c. The reduction of K decreases the viscous friction, so that the surges quickly reach a high velocity during the inertial regime. In turn, this leads to the sum of pressure gradient and weight becoming less than the yield stress within the flow, resulting in a negative source term in the momentum (4.34). Once inertia becomes negligible, the flow exhibits a rapid deceleration, ending with a non-trivial shape at stoppage. In this flow scenario, only two regimes are observed, namely the inertially dominated regime and the plasticity-dominated regime with a quick stoppage. The intermediate lubrication regime is not visible. This result illustrates the ability of our model to predict various stoppage shapes, which can be important for applications. Further studies could be conducted to systematically investigate the final deposit shapes as a function of the different flow parameters.

6. Selection of the consistent model

As shown in the previous section, the consistent shallow-flow model (4.33)–(4.35) produces realistic predictions in different flow configurations. However, an infinite number

https://doi.org/10.1017/jfm.2026.11662 Published online by Cambridge University Press

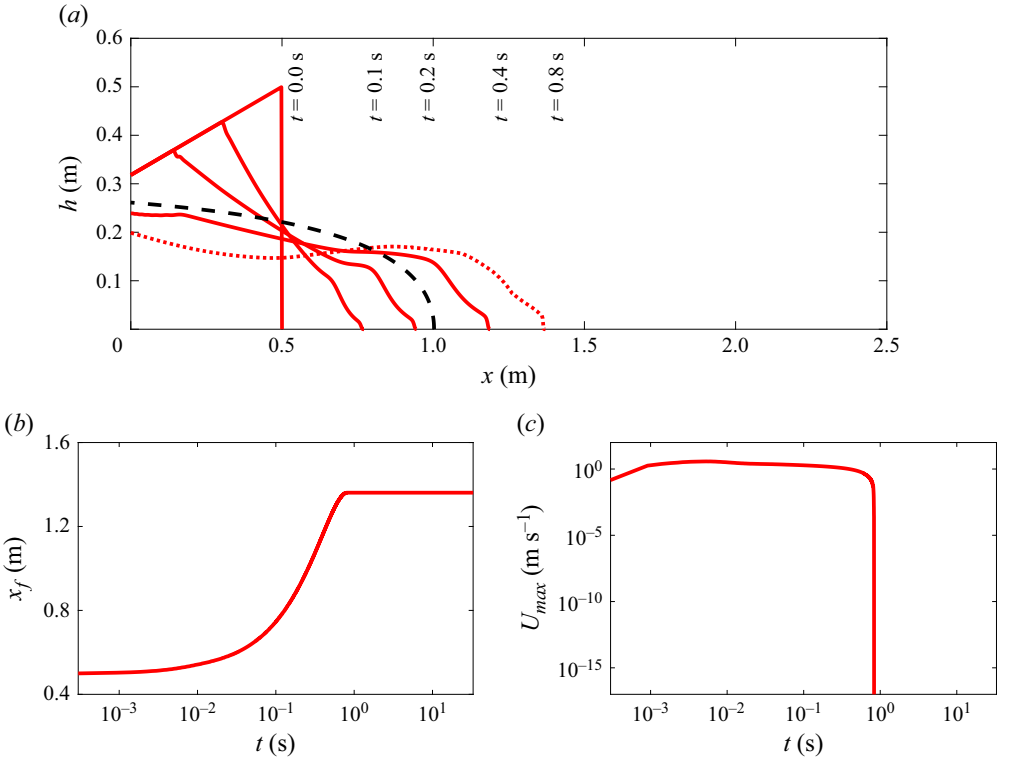


Figure 10. Dam-break simulation and final stoppage. Same legend as figure 9. Parameters are $\tau_c = 1000$ Pa, $K = 2$ Pa s^n, $n = 0.4$, $\theta = 20°$ and $\rho = 1000$ kg m^{-3}.

of consistent models can be derived from the asymptotic expansions (see § 4), which are all formally equivalent at $O(\varepsilon)$. In Appendix F, we present an alternative consistent model that differs from (4.33)–(4.35) in the formulation of the viscous friction term. In (4.33)–(4.35), this term is expressed by a nonlinear function of the velocity as $\alpha_1(n)\nu(U/h)|U/h|^{n-1}$. Instead, in the alternative model (F1)–(F3), the viscous friction is expressed as $(g\sin\theta)^{1-1/n}\hat{\alpha}_1(n)\nu\, U/h^{1+1/n}$, i.e. it depends linearly on the velocity. The question of the selection of the best-suited consistent model for flow simulations should thus be addressed. In this section, we illustrate the differences between the models and propose a selection method based on considering steady-state surges on an inclined plane. In this configuration inertia does not play any role, so that a proper shallow-flow model is expected to produce a similar result as the inertialess lubrication model given by

$$\frac{n}{1+2n}\left(\lambda - \frac{\varepsilon Re}{Fr^2}\frac{\partial h}{\partial x}\right)^{\frac{1}{n}} h^{\frac{n+1}{n}}\left[1 - \frac{Bi}{h}\left(\lambda - \frac{\varepsilon Re}{Fr^2}\frac{\partial h}{\partial x}\right)^{-1}\right]^{\frac{n+1}{n}} \times\left[1 + \frac{n}{(n+1)}\frac{Bi}{h}\left(\lambda - \frac{\varepsilon Re}{Fr^2}\frac{\partial h}{\partial x}\right)^{-1}\right] = U_s, \tag{6.1}$$

where U_s is the constant dimensionless surge propagation velocity. This ordinary differential equation for h results from the balance between gravity, hydrostatic pressure, yield stress and viscous friction (Liu *et al.* 2019; Chambon *et al.* 2020).

We can thus compare different consistent shallow-flow models with the lubrication model in the case of steady-state surges. Additionally, we compare our results with the

https://doi.org/10.1017/jfm.2026.11662 Published online by Cambridge University Press

Exp.	τ_c	K	ρ	n	θ	h_0	Bi	Re	Fr	λ	h_p
Carbopol	8.0	6.0	1000	0.43	15.3	15.5	0.5	1.37	0.39	2.455	0.20
Kaolin	10.8	13.1	1399	0.24	15.0	12.0	1.13	0.044	0.061	3.219	0.35

Table 1. Parameters of the experiments reported in Chambon *et al.* (2009, 2020): yield stress τ_c (Pa), consistency K (Pa s^n), density ρ (kg m^{-3}), power-law index n, slope angle θ (deg.), steady uniform height h_0 (mm), Bingham number Bi, Reynolds number Re, Froude number Fr, driving parameter λ, scaled theoretical pseudoplug thickness h_p.

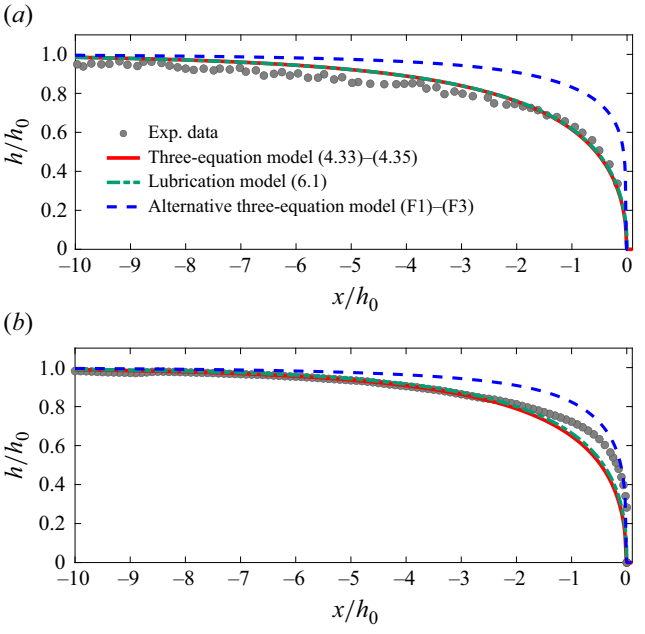


Figure 11. Simulated free-surface shapes of steady-state surges for the parameters indicated in table 1: (*a*) kaolin; (*b*) Carbopol. The red curve corresponds to the consistent three-equation model (4.33)–(4.35), the blue curve to the alternative consistent three-equation model (F1)–(F3) and the green curve to the lubrication model (6.1). The dots represent the experimental data of Chambon *et al.* (2009, 2020).

experiments for kaolin and Carbopol reported by Chambon *et al.* (2009, 2020). The parameters of these experiments are indicated in table 1. In the experiments the steady-state surges are generated by using a conveyor belt set-up. In the computation, these steady flows are generated by considering a large simulation domain $-50 \leqslant x/h_0 \leqslant 0$ with the following initial and boundary conditions: (i) at $t = 0$ the fluid occupies only the left part of the domain $-50 \leqslant x/h_0 \leqslant -25$, initiating a dam-break-like scenario with prescribed equilibrium flow solutions for all variables ($h = h_0$, $U = U^{(0)}$, $\varphi = \varphi^{(0)}$); (ii) at the upstream boundary $x = -50$, we impose the same equilibrium flow $h = h_0$, $U = U^{(0)}$, $\varphi = \varphi^{(0)}$ for any t; (iii) at the downstream boundary $x = 0$, a dry region is considered where all variables and fluxes are equal to zero. The flow is considered to have reached the steady-state regime once the depth-averaged velocity is equal to $U^{(0)}(h_0)$ everywhere within the surges.

Figure 11 shows comparisons between the different models and the experiments in terms of free-surface shape. The shallow-flow model (4.33)–(4.35) provides almost identical

https://doi.org/10.1017/jfm.2026.11662 Published online by Cambridge University Press

results as the lubrication model. Furthermore, both models are relatively close to the experimental data. In contrast, the alternative shallow-flow model (F1)–(F3) markedly deviates from the lubrication solution and from the experimental data, particularly for small values of n. Hence, even though both models are formally equivalent, they provide significantly different solutions in this case. We propose using the capability to reproduce the lubrication solution as a selection criterion among the possible shallow-flow models. In the case of (4.33)–(4.35), the agreement with the lubrication solution is obtained by formulating a viscous term that 'resembles' the Herschel–Bulkley viscous-stress tensor $K\dot{\boldsymbol{\gamma}}|\dot{\boldsymbol{\gamma}}|^{n-1}$ with $\dot{\boldsymbol{\gamma}} \sim U/h$. This is not the case for the model (F1)–(F3). Note that the two-equation shallow-flow model recently proposed by Muchiri *et al.* (2024) also includes a viscous friction term that is linearly dependent on U. It is thus likely that this model suffers from the same drawback as (F1)–(F3) for simulating steady-state surges. The first relaxation term in (4.34) at $\varphi \to 0$ can instead be proposed as an effective closure for formulating an inconsistent two-equation model.

7. Conclusions

A consistent shallow-flow model for viscoplastic fluid flows is derived by using smooth asymptotic expansions that are based on an alternative tensorial formulation of the Herschel–Bulkley constitutive law. The model consists of three equations: mass conservation, momentum balance and enstrophy. The final system has a fully hyperbolic structure. The source terms are adapted to capture dry fronts and flow stoppage. The numerical resolution is based on a Godunov scheme with the Rusanov solver, in which the hydrostatic pressure is considered as a source term. The latter ingredient is particularly important to adequately describe the behaviour of the viscoplastic fluid near the plastic limit at low speeds, and to capture stoppage of the material. The derived model also includes an additional parameter δ that arises from a specific regularization of the power-law viscous-stress tensor at first order. The parameter δ is related to the shearing in the pseudoplug: for $\delta = 0$ the model formally predicts no shearing in the pseudoplug in the z-direction.

The linear stability of the model is investigated, showing a stabilizing effect of plasticity. For $\delta = 0$, the result coincides with the criterion obtained by Balmforth & Liu (2004) for a model with zero shearing in the pseudoplug, as expected. The shear-thinning effect, i.e. decreasing the power-law index n, leads to a destabilizing effect for low yield stress values and to a stabilizing effect at large yield stress values. The linear stability threshold is found to be in good agreement with the experimental results of Noma *et al.* (2021). When this threshold is exceeded, long-wave perturbations of the uniform flows lead to the appearance of roll waves. The larger the yield stress is, the smaller the amplitude and wavelength of these roll waves. A decrease of n leads to a smaller wavelength and to a larger (respectively, smaller) amplitude for low (respectively, high) values of yield stress. The influence of the shearing in the pseudoplug, i.e. of the parameter δ, is also investigated, showing a slight decrease of the amplitude of the roll waves when δ increases. Nevertheless, this effect of δ is very small, which could justify the use of a model with zero shearing in the pseudoplug for practical applications.

Solutions of the dam-break problem are computed. The dynamics of the flow is compared with the experimental results of Ancey & Cochard (2009). At large slope angles, good agreement is found both in terms of front position and depth profiles. Unlike the lubrication model, the three-equation shallow-flow model properly captures the early stage of the flow, when inertia is the dominant driving force. A slight systematic shift in front position is observed, probably due to sidewall friction. At small slope angles,

https://doi.org/10.1017/jfm.2026.11662 Published online by Cambridge University Press

the comparison between the model and the experiments is less convincing, which may be due to a slight basal slip of the experimental fluid. Because the hydrostatic pressure is considered as a source term in the numerical scheme, the derived model can also adequately capture the behaviour of the viscoplastic flows at low velocity, as well as the stoppage of the material. It is shown that the final static mass can reach an arbitrary shape depending on the rheological parameters, although in simple cases the final shape coincides with the classical expression for the deposits.

An important question concerns the selection of the source terms in the final model, as different consistent expressions of these terms are possible, which are formally equivalent at $O(\varepsilon)$. A criterion is proposed, based on considering steady-state surge solutions. In such a configuration, the shallow-flow model is expected to provide results close to the inertialess lubrication model. It is found that the proposed consistent shallow-flow model, with a viscous friction term nonlinearly dependent on U, is effectively in good agreement with the lubrication model as well as with experimental results. On the contrary, an alternative consistent model with a viscous friction term linearly dependent on U, clearly overestimates the slope of the surge front in comparison with the lubrication model and the experiments.

In summary, the new three-equation model properly captures the instability threshold, and the numerical simulations conducted for roll waves, steady-state surges and the dam-break problem are found in good quantitative agreement with experimental data. An important advantage of this model is its ability to predict the stopping of the fluid under certain conditions. Comparisons with simpler lubrication models also show the benefits of properly including inertia effects. Although the derived three-equation model allows for an efficient and well-balanced numerical implementation, the algebraic complexity of the source terms naturally raises the question of which components are essential for accurately capturing the physics of viscoplastic flows. This consideration may become especially relevant in future extensions to three-dimensional flows, where the enstrophy variable becomes a tensor and the computational cost associated with the source terms may increase significantly. The derived model can thus be viewed as a reference framework, against which simpler and more computationally practical models can be developed and assessed. In particular, detailed comparisons with two-equation shallow-flow models would need to be conducted, in order to better understand the advantages of the three-equation approach for viscoplastic flows. Let us recall, however, that consistent two-equation models for viscoplastic fluids demonstrate a more complicated mathematical structure. Regarding other future developments, several improvements would also make the proposed model more useful for practical applications. First, inclusion of diffusion terms, even in a semiconsistent way, could improve the prediction of roll waves and sharp fronts. Second, the inclusion of an uneven bottom topography should be considered.

Acknowledgements. This work has received funding from the European Union's Horizon 2020 research and innovation programme under the Marie Sklodowska-Curie grant agreement No. 955605.

Declaration of interests. The authors report no conflict of interest.

Appendix A. The expressions of asymptotic expansion

The leading-order terms of the stress components, longitudinal velocity and pressure read

$$\tau_{xz}^{(0)} = \frac{\lambda}{Bi}(h - z), \tag{A1}$$

https://doi.org/10.1017/jfm.2026.11662 Published online by Cambridge University Press

$$\tau_{xz}^{v(0)} = \begin{cases} \dfrac{\lambda}{Bi}(h - z - h_p), & z < h - h_p, \\ 0, & z \geqslant h - h_p, \end{cases} \tag{A2}$$

$$\tau_{xz}^{Y(0)} = \begin{cases} 1, & z < h - h_p, \\ \dfrac{\lambda}{Bi}(h - z), & z \geqslant h - h_p, \end{cases} \tag{A3}$$

$$\tau_{xx}^{(0)} = \tau_{xx}^{Y(0)} = \begin{cases} 0, & z < h - h_p, \\ \operatorname{sgn}\{\tau_{xx}\}\sqrt{1 - \left(\dfrac{h - z}{h_p}\right)^2}, & z \geqslant h - h_p, \end{cases} \tag{A4}$$

$$u^{(0)} = \begin{cases} \dfrac{n}{1+n}\lambda^{1/n}\left[\left(h - h_p\right)^{1+1/n} - \left(h - h_p - z\right)^{1+1/n}\right], & z < h - h_p, \\ \dfrac{n}{1+n}\lambda^{1/n}\left(h - h_p\right)^{1+1/n}, & z \geqslant h - h_p, \end{cases} \tag{A5}$$

$$p^{(0)} = \begin{cases} h - z, & z < h - h_p, \\ h - z - \operatorname{sgn}\{\tau_{xx}\}Bi\dfrac{Fr^2}{Re}\sqrt{1 - \left(\dfrac{h - z}{h_p}\right)^2}, & z \geqslant h - h_p. \end{cases} \tag{A6}$$

To derive a consistent model at $O(\varepsilon)$, the expression of the leading-order normal velocity $w^{(0)}$ is only needed for $z < h - h_p$:

$$w^{(0)} = \lambda^{1/n}\left\{\frac{n}{1+n}\left[\left(h - h_p\right)^{1+1/n} - \left(h - h_p - z\right)^{1+1/n}\right] - z\left(h - h_p\right)^{1/n}\right\}\frac{\partial h}{\partial x}. \tag{A7}$$

The zone $z < h - h_p$ corresponds to the fully sheared layer with $\partial u/\partial z = O(1)$, while the zone $h > z > h - h_p$ corresponds to a pseudoplug layer in which $\partial u/\partial z = O(\varepsilon)$. The thickness of the pseudoplug h_p is given by

$$h_p = \frac{Bi}{\lambda}. \tag{A8}$$

In the sheared layer, for $z < h - h_p$, viscous stresses are given by

$$\begin{aligned} \tau_{xz}^{v(1)} = {} & \frac{\lambda^{1/n}Re}{Bi}\left\{\frac{h - h_p - z}{1+n}\left[n\left(h - h_p - z\right)^{1/n} - (1+n)\left(h - h_p\right)^{1/n}\right]\right. \\ & \left. - h_p\left(h - h_p\right)^{1/n}\right\}\frac{\partial h}{\partial t} + \frac{Re}{Bi}\left\{\frac{z - h}{Fr^2} + \frac{n}{(1+n)(1+2n)}\lambda^{2/n}\left(h - h_p\right)^{1/n} \times \right. \\ & \left.\left[\left(h - h_p - z\right)^{1+1/n}\left(2n\left(h - h_p\right) + z\right) - (1+2n)(h - z)\left(h - h_p\right)^{1+1/n}\right]\right\}\frac{\partial h}{\partial x} \end{aligned} \tag{A9}$$

while in the pseudoplug, for $z > h - h_p$:

$$\tau_{xz\mathrm{PP}}^{v(1)} = \frac{Re}{Bi}(z - h)\left[\lambda^{1/n}\left(h - h_p\right)^{1/n}\frac{\partial h}{\partial t} + \left(\frac{1}{Fr^2} + \frac{n}{1+n}\lambda^{2/n}\left(h - h_p\right)^{1+2/n}\right)\frac{\partial h}{\partial x}\right]. \tag{A10}$$

The yield-stress part of the shear stress simply expresses as $\tau_{xz}^{Y(1)} = 2\tau_{xx}^{Y(0)}\partial h/\partial x$.

https://doi.org/10.1017/jfm.2026.11662 Published online by Cambridge University Press

The first-order correction to the longitudinal velocity is given by

$$u^{(1)} = I_T(x,z,t)\frac{\partial h}{\partial t} + \Big[I_X(x,z,t) + P(x,z,t)\Big]\frac{\partial h}{\partial x}, \tag{A11}$$

where the terms I_T and I_X relate to the inertial contributions, and the term P relates to the pressure contribution. In the sheared layer, for $z < h - h_p$, these terms are given by

$$\begin{aligned} I_T(x,z,t) = \frac{Re\lambda^{-1+2/n}}{(n+1)(n+2)}\Big\{ & -n\left(h-h_p-z\right)^{1+2/n} - \left(h-h_p\right)^{2/n}\left[n\left(n+3\right)h_p + 2h\right] \\ & + (n+2)\left(h-h_p\right)^{1/n}\left(h-h_p-z\right)^{1/n}\left(nh_p + h - z\right) \\ & + \delta^{\frac{1-n}{n}}\frac{n+2}{2n+1}\left(n\left(h-h_p\right)^{\frac{1}{n}+2} - n\left(-h_p+h-z\right)^{\frac{1}{n}+2}\right) \\ & + \delta^{\frac{1-n}{n}}\frac{z}{2n}(n+1)(n+2)(z-2h)\left(h-h_p\right)^{\frac{1}{n}}\Big\}, \end{aligned} \tag{A12}$$

$$\begin{aligned} I_X(x,z,t) = \frac{nRe\lambda^{-1+3/n}}{2\left(n+1\right)^2\left(n+2\right)\left(2n+1\right)}\Big\{ & \left(h-h_p\right)^{1/n}\left(h-h_p-z\right)^{1/n} \times \\ & \Big[2\left(n+2\right)\left(2n+1\right)\left(h-h_p\right)^{1+1/n}\left(h-z+nh_p\right) \\ & - \left(h-z-h_p\right)^{1+1/n}\left(n\left(5+4n\right)\left(h-h_p\right) + \left(2+n\right)z\right)\Big] \\ & - \left(h-h_p\right)^{1+3/n}\Big[\left(4+5n\right)h + n\left(9+14n+4n^2\right)h_p\Big] \\ & + \frac{\delta^{\frac{1-n}{n}}}{n}(n+1)(n+2)(2n+1)z(z-2h)\left(h-h_p\right)^{\frac{2}{n}+1} \\ & + \delta^{\frac{1-n}{n}}\Big[\left(h_p-h+z\right)^2\left(\left(h_p-h\right)\left(h_p-h+z\right)\right)^{\frac{1}{n}}\left(3nh_p - 3hn - z\right) \\ & + 3n\left(h-h_p\right)^{\frac{2}{n}+3}\Big] \times \frac{2(n+1)(n+2)(2n+1)}{n(6n+5)+1}\Big\}, \end{aligned} \tag{A13}$$

$$\begin{aligned} P(x,z,t) = \frac{Re\lambda^{-1+1/n}}{(n+1)Fr^2}\Big[& \left(h-h_p-z\right)^{1/n}\left(h+nh_p-z\right) - \left(h-h_p\right)^{1/n}\left(h+nh_p\right) \\ & + \frac{\delta^{\frac{1-n}{n}}(n+1)}{2n}z(z-2h)\Big]. \end{aligned} \tag{A14}$$

In the pseudoplug, for $z > h - h_p$, the expressions are

$$\begin{aligned} I_T(x,z,t) = \frac{Re\lambda^{-1+2/n}}{(1+n)}\Big\{ & -\frac{\left(h-h_p\right)^{2/n}\left[n\left(n+3\right)h_p + 2h\right]}{n+2} \\ & + \frac{\delta^{\frac{1-n}{n}}}{2n(2n+1)}\left(h-h_p\right)^{\frac{1}{n}}\Big[-2h\left(-hn^2 + n\left(2n\left(h_p+z\right)+3z\right)+z\right) \\ & + 2n^2h_p^2 + (n+1)(2n+1)z^2\Big]\Big\}, \end{aligned} \tag{A15}$$

https://doi.org/10.1017/jfm.2026.11662 Published online by Cambridge University Press

$$I_X(x,z,t)=\frac{Re\left(h-h_p\right)^{1/n}\lambda^{-1+3/n}}{2\,(n+1)^2\,(n+2)\,(2n+1)}\Big\{\Big[n\left(h-h_p\right)^{2/n}\left[n\,(2n\,(2n+7)+9)\,h_p\right.$$
$$\left.+h\,(5n+4)\right]\Big]\left(h_p-h\right)+\frac{\delta^{\frac{1-n}{n}}}{3n+1}(n+1)(n+2)\left(h-h_p\right)^{\frac{1}{n}+1}\Big[(n(6n+5)+1)z^2$$
$$+6n^2h_p^2-2h\left(-3hn^2+n\left(6n\left(h_p+z\right)+5z\right)+z\right)\Big]\Big\},\tag{A16}$$

$$P(x,z,t)=\frac{Re\lambda^{-1+1/n}}{(n+1)\,Fr^2}\Big\{-\left(h-h_p\right)^{1/n}\left(nh_p+h\right)+\frac{\delta^{\frac{1-n}{n}}(n+1)}{2n}z(z-2h)\Big\}.\tag{A17}$$

Using (4.6) with the definitions $\xi=h_p/h$ and $\zeta=\delta/h$, the first-order correction to the depth-averaged velocity is given by

$$\frac{U^{(1)}}{Re}=\Big[\frac{\lambda^{\frac{3-n}{n}}h^{\frac{2n+3}{n}}(1-\xi)^{3/n}}{(2+n)(2+3n)(1+n)^2(1+2n)}\Big[n\Big(n^2(n(6n+19)+11)\xi^3$$
$$+2n(n(6n+19)+11)\xi^2+(n+2)(9n+7)\xi+2(n(n+4)+5)\Big)+4\Big]$$
$$-\frac{\lambda^{\frac{3-n}{n}}h^{\frac{2n+3}{n}}\zeta^{\frac{1-n}{n}}(1-\xi)^{2/n}}{3n(1+n)(1+2n)(1+3n)(1+4n)}\Big[(\xi(3\xi(4\xi-5)-32)-15)n^3$$
$$+12\xi^2\left(\xi^2-3\right)n^4+(3(\xi-5)\xi-23)n^2-(\xi+9)n-1\Big]$$
$$-\frac{\lambda^{\frac{1-n}{n}}h^{\frac{1+n}{n}}}{Fr^2}\left(\frac{1}{3n}+\frac{(2n\xi\,(n\xi+1)+n+1)\,(1-\xi)^{\frac{1}{n}}}{(n+1)(2n+1)}\right)\Big]\frac{\partial h}{\partial x},\tag{A18}$$

while the first-order correction to the enstrophy reads as

$$\frac{\varphi^{(1)}}{Re}=\frac{n(1-\xi)^{\frac{1+n}{n}}}{3(n+1)^3(2n+1)^2}\Big[\frac{n\lambda^{\frac{4-n}{n}}h^{\frac{4+n}{n}}(1-\xi)^{\frac{3}{n}}}{(2+n)(2+3n)(3+4n)}\Big[n\Big(6n^2(4n+3)(n(6n+19)+11)\xi^3$$
$$+n(n(8n(27n+110)+967)+322)\xi^2+(n+2)(20n(7n+11)+87)\xi$$
$$+18(n(n(n+5)+9)+7)\Big)+36\Big]-\frac{\lambda^{\frac{4-n}{n}}h^{\frac{4+n}{n}}\zeta^{\frac{1-n}{n}}(n+1)(1-\xi)^{2/n}}{(1+3n)(1+4n)(2+5n)}\Big[n\Big(24n^3(5n+2)\xi^4$$
$$-3n^2(n(80n+13)-7)\xi^3-6n(n(4n(5n+16)+29)+3)\xi^2$$
$$-(n+1)(n(179n+108)+16)\xi-2(n(n(21n+55)+49)+17)\Big)-4\Big]$$
$$-\frac{\lambda^{\frac{2-n}{n}}h^{\frac{2}{n}(n+1)}}{Fr^2(3n+1)(3n+2)(4n+1)}\Big[2\zeta^{\frac{1-n}{n}}(n+1)(n(6n+7)+2)\left(n\left(3n(\xi+1)^2+3\xi+4\right)+1\right)$$
$$+3n(3n+1)(4n+1)\Big(n\xi(2n((6n+4)\xi+5)+7)+2n(n+2)+2\Big)(1-\xi)^{\frac{1}{n}}\Big]\Big]\frac{\partial h}{\partial x}.\tag{A19}$$

Appendix B. The coefficients for the main model

The coefficients for the main model are as follows:

https://doi.org/10.1017/jfm.2026.11662 Published online by Cambridge University Press

$$C_1(n,\xi,\zeta)=\frac{2\xi n(n\xi+1)+n+1}{2n+1}+\Bigg[\frac{\zeta^{\frac{1-n}{n}}(n+1)}{(3n+1)(4n+1)}\Big(12\xi^2\left(\xi^2-3\right)n^4$$
$$+(\xi(3\xi(4\xi-5)-32)-15)n^3+(3(\xi-5)\xi-23)n^2-(\xi+9)n-1\Big)$$
$$-\frac{3n(1-\xi)^{\frac{1}{n}}}{(n+2)(3n+2)}\Big(n\big(n^2(n(6n+19)+11)\xi^3+2n(n(6n+19)+11)\xi^2$$
$$+(n+2)(9n+7)\xi+2(n(n+4)+5)\big)+4\Big)\Bigg]$$
$$\times\left(\zeta^{\frac{1-n}{n}}(n+1)(2n+1)+3n(2\xi n(n\xi+1)+n+1)(1-\xi)^{\frac{1}{n}}\right)^{-1};\quad\text{(B1)}$$

$$C_2(n,\xi)=\frac{n^2\xi(1-\xi)^{\frac{2}{n}+1}\left(n\left((3\xi(\xi+1)+2)n^2+2(\xi+1)(\xi+3)n+4\xi+6\right)+2\right)}{(n+1)^2(2n+1)^2(3n+2)};\quad\text{(B2)}$$

$$C_3(n,\xi,\zeta)=\frac{(n((3n+2)\xi+n+2)+1)^{\frac{n}{2}-1}}{3(1-\xi)^{1/n}(n+1)^{1+n}(2n+1)^n}\Bigg((1-\xi)^{\frac{2}{n}+1}\Bigg[\frac{n(1-\xi)^{\frac{1}{n}}}{(n+2)(3n+2)(4n+3)}$$
$$\times\Big[n\big(6n^2(4n+3)(n(6n+19)+11)\xi^3+n(n(8n(27n+110)+967)+322)\xi^2$$
$$+(n+2)(20n(7n+11)+87)\xi+18(n(n(n+5)+9)+7)\big)+36\Big]$$
$$-\frac{\zeta^{\frac{1-n}{n}}(n+1)}{(3n+1)(4n+1)(5n+2)}(n(24n^3(5n+2)\xi^4-3n^2(n(80n+13)-7)\xi^3$$
$$-6n(n(4n(5n+16)+29)+3)\xi^2-(n+1)(n(179n+108)+16)\xi$$
$$-2(n(n(21n+55)+49)+17))-4)\Bigg]+\Bigg[(2n+1)(1-\xi)^{\frac{2}{n}+1}\times$$
$$\times\Bigg[\frac{\zeta^{\frac{1-n}{n}}(n+1)}{(3n+1)(4n+1)}\Big(12\xi^2(\xi^2-3)n^4+(\xi(3\xi(4\xi-5)-32)-15)n^3$$
$$+(3(\xi-5)\xi-23)n^2-(\xi+9)n-1\Big)-\frac{3n(1-\xi)^{\frac{1}{n}}}{(n+2)(3n+2)}\Big((6n^5+19n^4+11n^3)\xi^3$$
$$+2(6n^4+19n^3+11n^2)\xi^2+(n^2+2n)(9n+7)\xi+2(n^2(n+4)+5n)+4\Big)\Bigg]$$
$$\times\Big[2\zeta^{\frac{1-n}{n}}(n+1)(n(3(3\xi(\xi(\xi+3)-1)-1)n^3+2(3\xi(\xi(\xi+6)+2)-2)n^2+6\xi+4$$
$$+3n^2(3n+1)(4n+1)\xi((4n+3)\xi n+n+1)(1-\xi)^{\frac{1}{n}}+(3\xi(4\xi+7)+2)n)+1)\Big]\Bigg]$$
$$\times\Bigg[(3n+1)(3n+2)(4n+1)(\xi n+n+1)(\zeta^{\frac{1-n}{n}}(n+1)(2n+1)+3n(2\xi n(n\xi+1)$$
$$+n+1)(1-\xi)^{\frac{1}{n}})\Bigg]^{-1}+\frac{(\xi-1)(n((3n+2)\xi+n+2)+1)}{(3n+2)(\xi n+n+1)}\Bigg[\frac{6n(1-\xi)^{3/n}}{(n+2)(3n+2)}$$
$$\times\Big(n(n^2(n(6n+19)+11)\xi^3+2n(n(6n+19)+11)\xi^2+(n+2)(9n+7)\xi$$

https://doi.org/10.1017/jfm.2026.11662 Published online by Cambridge University Press

$$+2(n(n+4)+5))+4\Big]-\frac{2\zeta^{\frac{1-n}{n}}(n+1)(1-\xi)^{2/n}}{(3n+1)(4n+1)}\Big(12\xi^2(\xi^2-3)n^4+(\xi(3\xi(4\xi-5)-32)-15)n^3+(3(\xi-5)\xi-23)n^2-(\xi+9)n-1\Big)\Big]\Big)(3n+2)^{1-\frac{n}{2}}(n-n\xi)^{\frac{3n-4}{2}};\tag{B3}$$

$$C_4(n,\xi,\zeta)=\frac{(1+3n+2n^2)^{2-n}}{(1-\xi)^{\frac{3n^2-2n-2}{2n}}n^{\frac{2-3n}{2}}}\Big[2\zeta^{\frac{1-n}{n}}(n+1)\Big(n(3(3\xi(\xi(\xi+3)-1)-1)n^3+2(3\xi(\xi(\xi+6)+2)-2)n^2+(3\xi(4\xi+7)+2)n+6\xi+4)+1\Big)+3n^2(3n+1)(4n+1)\xi((4n+3)\xi n+n+1)(1-\xi)^{\frac{1}{n}}\Big]\times\Big[(n+1)(3n+1)(3n+2)(4n+1)(\xi n+n+1)\Big(\zeta^{\frac{1-n}{n}}(n+1)(2n+1)+3n(2\xi n(n\xi+1)+n+1)(1-\xi)^{\frac{1}{n}}\Big)\Big]^{-1}\Big(\frac{3n+2}{n((3n+2)\xi+n+2)+1}\Big)^{1-\frac{n}{2}};\tag{B4}$$

$$C_5(n,\xi,\zeta)=\Big[\frac{6n(1-\xi)^{3/n}}{(n+2)(3n+2)}\Big(n(n^2(n(6n+19)+11)\xi^3+(n+2)(9n+7)\xi+2n^2+8n+10+2n(n(6n+19)+11)\xi^2)+4\Big)-\frac{2\zeta^{\frac{1-n}{n}}(n+1)(1-\xi)^{2/n}}{(3n+1)(4n+1)}\Big(12\xi^2\left(\xi^2-3\right)n^4+(\xi(3\xi(4\xi-5)-32)-15)n^3+(3(\xi-5)\xi-23)n^2-(\xi+9)n-1\Big)\Big]\times\Big[2\zeta^{\frac{1-n}{n}}(n+1)^2(2n+1)+6n(n+1)(2\xi n(n\xi+1)+n+1)(1-\xi)^{\frac{1}{n}}\Big]^{-1}-\frac{(1-\xi)^{2/n}(n\xi(n(3(4n+3)\xi+13)+10)+4n(n+2)+4)}{2(n+1)(3n+2)(\xi n+n+1)};\tag{B5}$$

$$C_6(n,\xi,\zeta)=\frac{-n(1-\xi)^{2/n}}{2(n+1)^2(2n+1)^2(3n+2)(\xi n+n+1)}\Big[\xi\Big(3\xi(\xi(\xi(2\xi+5)+7)-7)-5\Big)n^5+\Big(\xi(\xi(\xi(4\xi(\xi+7)+77)-25)-26)-2\Big)n^4+(\xi(\xi+1)(12\xi(\xi+5)-31)-6)n^3+(\xi(\xi(20\xi+41)-5)-6)n^2+(\xi(11\xi+7)-2)n+2\xi\Big];\tag{B6}$$

$$\beta_1(n,\xi,\zeta)=\frac{3n(n+1)^n\left((1-\xi)^{\frac{1}{n}+1}(\xi n+n+1)\right)^{1-n}}{\zeta^{\frac{1-n}{n}}(n+1)(2n+1)+3n(2\xi n(n\xi+1)+n+1)(1-\xi)^{\frac{1}{n}}}+\frac{C_4(n,\xi,\zeta)\big(C_2(n,\xi)+C_1(n,\xi,\zeta)\big)(1-\xi)^{\frac{1-n^2}{n}}(\xi n+n+1)^{1-n}}{C_3(n,\xi,\zeta)(2n+1)(n+1)^{1-n}};\tag{B7}$$

https://doi.org/10.1017/jfm.2026.11662 Published online by Cambridge University Press

$$\Gamma_1(n,\xi,\zeta)=\frac{3n(n+1)^n\left((1-\xi)^{\frac{1}{n}+1}(\xi n+n+1)\right)^{1-n}}{\zeta^{\frac{1-n}{n}}(n+1)(2n+1)+3n(2\xi n(n\xi+1)+n+1)(1-\xi)^{\frac{1}{n}}}+\frac{C_4(n,\xi,\zeta)\big(C_6(n,\xi)+C_5(n,\xi,\zeta)\big)(1-\xi)^{\frac{1-n^2}{n}}(\xi n+n+1)^{1-n}}{C_3(n,\xi,\zeta)(2n+1)(n+1)^{1-n}};\tag{B8}$$

$$\beta_2(n,\xi,\zeta)=\frac{C_2(n,\xi)+C_1(n,\xi,\zeta)}{C_3(n,\xi,\zeta)};\tag{B9}$$

$$\Gamma_2(n,\xi,\zeta)=\frac{C_6(n,\xi)+C_5(n,\xi,\zeta)}{C_3(n,\xi,\zeta)};\tag{B10}$$

$$r_1(n,\xi,\zeta)=\Gamma_1(n,\xi,\zeta)-\beta_1(n,\xi,\zeta);\tag{B11}$$

$$r_2(n,\xi,\zeta)=\Gamma_2(n,\xi,\zeta)-\beta_2(n,\xi,\zeta).\tag{B12}$$

Appendix C. Well-balanced numerical scheme

The left-hand side of the system (4.33), (4.34) and (4.35) is fully hyperbolic, while the right-hand side corresponds to source terms given by algebraic expressions. The numerical resolution of such a system is usually based on two steps: (i) solution of the source-free system using a finite-volume Godunov-type scheme; (ii) integration of the source terms. Again, specific care should be taken to properly handle stoppage in the numerical scheme. If the hydrostatic pressure term $(g\cos\theta/2)\,\partial h^2/\partial x$ is included in the momentum flux in (4.34), the first step of the scheme will always generate a displacement of the free surface, even if the velocity is zero and the fluid depth satisfies the condition (4.32) everywhere. In fact, in the first step the hydrostatic pressure term affects the free surface as if there were no yield stress, and the resulting displacement is not compensated in the second step since the source term for the mass conservation is zero (see Appendix C.5). A possible way to overcome this difficulty is to account for weight and yield stress in the first step when solving the source-free system (Fernández-Nieto *et al.* 2023). In our work, we instead propose to consider the hydrostatic pressure as a source term in order to build a well-balanced numerical scheme.

The hyperbolic step requires solving a Riemann problem in every cell and at each time step (see e.g. Toro 1999). Here we present a numerical scheme for the model (4.33)–(4.35) based on the first-order Rusanov solver. This scheme can be applied to all the other models considered in this paper. Other approximate Riemann solvers, such as Harten–Lax–van Leer (HLL) and Harten–Lax–van Leer contact (HLLC), were found more challenging to implement if the hydrostatic pressure is taken as a source term.

C.1. *Vector form*

The model (4.33)–(4.35) can be written in a vector form

$$\frac{\partial \boldsymbol{V}}{\partial t}+\frac{\partial F(\boldsymbol{V})}{\partial x}=S(\boldsymbol{V}),\tag{C1}$$

https://doi.org/10.1017/jfm.2026.11662 Published online by Cambridge University Press

where the flow $\boldsymbol{V}$ and flux $F(\boldsymbol{V})$ vectors are defined as

$$\boldsymbol{V} = \begin{bmatrix} h \\ hU \\ h\varphi \end{bmatrix}, \qquad F(\boldsymbol{V}) = \begin{bmatrix} hU \\ hU^2 + 3h\varphi \\ hU\varphi \end{bmatrix}. \tag{C2}$$

The source vector is defined as $S(\boldsymbol{V}) = [0, S_m, S_e]$, where the momentum and the enstrophy source components S_m and S_e are readily obtained from (4.34) and (4.35).

The characteristics speeds, calculated as the eigenvalues of the matrix $F'(\boldsymbol{V})$, are given by

$$C_0(U) = U; \quad C^-(h, U, \varphi) = U - \sqrt{3h^2\varphi}; \quad C^+(h, U, \varphi) = U + \sqrt{3h^2\varphi}. \tag{C3}$$

C.2. *Hyperbolic step*

Let us define a fixed grid of size $\Delta x = x_{i+1/2} - x_{i-1/2}$ and the time increment $\Delta t = t^{N+1} - t^N$. The discrete values of the vector $\boldsymbol{V}(x, t)$ at (x_i, t^N) are denoted by $\boldsymbol{V}_i^N \equiv \boldsymbol{V}(x_i, t^N)$. The hyperbolic step consists of integrating the source-free system ($S(\boldsymbol{V}) = 0$), resulting in the following conservative finite-volume Godunov scheme:

$$\tilde{\boldsymbol{V}}_i^{N+1} = \boldsymbol{V}_i^N - \frac{\Delta t}{\Delta x}\left(\boldsymbol{F}_{i+1/2}^{*,N} - \boldsymbol{F}_{i-1/2}^{*,N}\right). \tag{C4}$$

Here $\boldsymbol{F}_{i+1/2}^{*,N}$ and $\boldsymbol{F}_{i-1/2}^{*,N}$ are the Godunov numerical fluxes across the interfaces between cells. To compute these fluxes, Riemann problems between the cells i, $i+1$ and $i-1$, i, respectively, have to be solved. The exact solutions of such problems are rather complicated. Several approximate Riemann solvers have been developed (Toro 1999). Here, we use the Rusanov solver, in which the numerical fluxes are approximated as

$$\boldsymbol{F}_{i+1/2}^{*,N} = \frac{1}{2}\left(\boldsymbol{F}_i^N + \boldsymbol{F}_{i+1}^N\right) - \frac{C_{i+1/2}^{max}}{2}\left(\boldsymbol{V}_{i+1}^N - \boldsymbol{V}_i^N\right), \tag{C5}$$

where $C_{i+1/2}^{max}$ is given through the characteristic speeds C^+ and C^- defined in (C3):

$$C_{i+1/2}^{max} = \max\left(|C_i^{+,N}|, |C_i^{-,N}|, |C_{i+1}^{+,N}|, |C_{i+1}^{-,N}|\right). \tag{C6}$$

Substitution of (C5)–(C6) into the Godunov scheme (C4) allows calculating the intermediate flow vector $\tilde{\boldsymbol{V}}_i^{N+1}$. As the Godunov scheme is only conditionally stable, the increment Δt must respect the Courant–Friedrichs–Lewy condition (Toro 1999).

C.3. *Integration of the source terms*

The second step consists of solving the following equation:

$$\frac{\boldsymbol{V}_i^{N+1} - \tilde{\boldsymbol{V}}_i^{N+1}}{\Delta t} = S(\boldsymbol{V}), \tag{C7}$$

where $\tilde{\boldsymbol{V}}_i^{N+1}$ is the intermediate flow vector computed at the first step. The source vector $\boldsymbol{S}$ can be evaluated at $\boldsymbol{V}_i^N$. In this case, (C7) can be integrated by an explicit scheme with a low computational cost. However, this scheme tends to be unstable when modelling flows over a dry bed. Instead, the source vector $\boldsymbol{S}$ can be evaluated at $\boldsymbol{V}_i^{N+1}$. This leads to an implicit scheme, which is unconditionally stable but requires the implementation of costly iterative methods. Here, we evaluate one part of the source vector at $\boldsymbol{V}_i^N$ and another part at

https://doi.org/10.1017/jfm.2026.11662 Published online by Cambridge University Press

$\boldsymbol{V}_i^{n+1}$. This mixed formulation allows us to avoid numerical instability close to dry fronts, but yet to have an analytical resolution of (C7) with respect to the unknown quantities h_i^{N+1}, U_i^{N+1} and φ_i^{N+1}. This yields the following system:

$$\frac{h_i^{N+1} - \tilde{h}_i^{N+1}}{\Delta t} = 0, \tag{C8}$$

$$\begin{aligned}
\frac{h_i^{N+1}U_i^{N+1} - \tilde{h}_i^{N+1}\tilde{U}_i^{N+1}}{\Delta t} &= -\frac{g\cos\theta}{2}\frac{\left(h_{i+1}^{N+1}\right)^2 - \left(h_{i-1}^{N+1}\right)^2}{2\Delta x} \\
&+ \left[gh_i^{N+1}\sin\theta\left(1 - q\left(n, \xi_i^{N+1}\right)\right) - \frac{\tau_c}{\rho} - \alpha_1(n)\nu\frac{U_i^{N+1}}{h_i^{N+1}}\left|\frac{U_i^N}{h_i^{N+1}}\right|^{n-1}\right] \\
&\times \left(1 + \left[\beta_1\left(n, \xi_i^{N+1}, \zeta_i^{N+1}\right) - 1\right] f\left(n, \varphi_i^N, \xi_i^{N+1}\right)\right) \\
&+ \left(\varphi_i^N\right)^{\frac{n-2}{2}}\left[\varphi_i^{N+1} - \alpha_2\left(n, \xi_i^{N+1}\right)\left(\frac{U_i^{N+1}}{h_i^{N+1}}\right)^2\right] \\
&\times \left(\beta_2^*(n) + \left[\beta_2\left(n, \xi_{i+1}^N, \zeta_i^{N+1}\right) - \beta_2^*(n)\right] f\left(n, \varphi_i^N, \xi_i^{N+1}\right)\right),
\end{aligned} \tag{C9}$$

$$\begin{aligned}
&\frac{h_i^{N+1}\varphi_i^{N+1} - \tilde{h}_i^{N+1}\tilde{\varphi}_i^{N+1}}{\Delta t} = \\
&\frac{2U_i^{N+1}}{\left(h_i^{N+1}\right)^2}\left[gh_i^{N+1}\sin\theta\left(1 - q\left(n, \xi_i^{N+1}\right)\right) - \frac{\tau_c}{\rho} - \alpha_1(n)\nu\frac{U_i^{N+1}}{h_i^{N+1}}\left|\frac{U_i^N}{h_i^{N+1}}\right|^{n-1}\right] \\
&\times r_1\left(n, \xi_i^{N+1}, \zeta_i^{N+1}\right) f\left(n, \varphi_i^N, \xi_i^{N+1}\right) \\
&+ \frac{2U_i^{N+1}\left(\varphi_i^N\right)^{\frac{n-2}{2}}}{\left(h_i^{N+1}\right)^2}\left[\varphi_i^{N+1} - \alpha_2\left(n, \xi_i^{N+1}\right)\left(\frac{U_i^{N+1}}{h_i^{N+1}}\right)^2\right] \\
&\times \left(\beta_2^*(n) + \left[\beta_2\left(n, \xi_i^{N+1}, \zeta_i^{N+1}\right) - \beta_2^*(n)\right] f\left(n, \varphi_i^N, \xi_i^{N+1}\right)\right).
\end{aligned} \tag{C10}$$

Equation (C8) gives $h_i^{N+1} = \tilde{h}_i^{N+1}$. The system (C9)–(C10) can then be solved analytically with respect to the unknowns U_i^{N+1} and φ_i^{N+1}. This yields two roots for each variable, but only one pair of solutions is physical.

C.4. *Dry front and yielding criterion*

To model flows with a dry front, it is necessary to specify the behaviour of the system when the computed variables reach small values close to the rounding error κ_n (in our simulations $\kappa_n \approx 10^{-16}$). If $h_i^N < \kappa_n$, we consider the cell to be dry, so that the velocity and enstrophy are zero: U_i^N and $\varphi_i^N = 0$. To satisfy mass conservation, the computed height value h_i^N is kept. To avoid division by zero, the variables U and φ are replaced by $U_i^N + \kappa_n$ and $\varphi_i^N + \kappa_n$ each time they appear in the denominators in the source terms.

https://doi.org/10.1017/jfm.2026.11662 Published online by Cambridge University Press

In terms of numerical variables, the yielding criterion is expressed as

$$\left| gh_i^{N+1}\sin\theta - \frac{g\cos\theta}{2}\frac{\left(h_{i+1}^{N+1}\right)^2-\left(h_{i-1}^{N+1}\right)^2}{2\Delta x} + \frac{h_i^{N+1}\tilde{U}_i^{N+1}}{\Delta t}\right| \leqslant \frac{\tau_c}{\rho} \;\Rightarrow\; (U_i^{N+1},\varphi_i^{N+1})=0. \tag{C11}$$

The first term corresponds to the weight, the second to the pressure gradient and the third relates to inertia with the value $\tilde{U}_i^{N+1}$ computed at the first step (C4). This yielding criterion is checked for each cell at the beginning of the second step. Integration of the source terms is performed only if the criterion is exceeded.

C.5. *The well-balanced property*

The Godunov flux in (C5) corresponds to a centred difference scheme with a numerical diffusion term $D_{i+1/2}^N = -C_{i+1/2}^{max}/2(\boldsymbol{V}_{i+1}^N - \boldsymbol{V}_i^N)$. This diffusive term, of order $O(\Delta x)$, ensures the stability of the scheme. At stoppage, when $(U,\varphi)=0$ and the flow depth satisfies inequality (4.32), the characteristics speeds (C3) are zero and the diffusive term $D_{i+1/2}^N$ naturally vanishes. This feature, together with the yielding criterion (C11), ensures the well-balanced property of the scheme. Note that considering the hydrostatic pressure as a source term is essential here. Otherwise, the characteristics speeds would be written as

$$\hat{C}_i^{\pm,N} = U_i^N \pm \sqrt{gh_i^N\cos\theta + 3\left(h_i^N\right)^2\varphi_i^N}, \tag{C12}$$

and at stoppage, the numerical diffusion in the mass equation would be $D_{i+1/2}^N = -\sqrt{g\max\{h_i^N,h_{i+1}^N\}\cos\theta}(h_{i+1}^N - h_i^N)$. This quantity is never zero if $\partial_x h \neq 0$, which would generate a non-physical displacement of the free-surface after stoppage. Moreover, as shown in § 5.3, this scheme with the hydrostatic pressure in the flux tends to induces numerical artefacts even at small velocities, as the diffusive term in the mass equation becomes dominant and leads to overestimating the evolution of the free surface. As a result, the classical Rusanov solver with the characteristics speeds given by (C12) is more diffusive than the well-balanced Rusanov solver with the characteristics speeds given by (C3).

It is possible to design a well-balanced scheme with the hydrostatic pressure taken as a part of the flux. However, it is then necessary to incorporate the weight and the yield stress into the first Godunov step. In particular, it includes methods based on the hydrostatic reconstruction of the flow depth, first proposed by Bouchut (2005) for viscous fluid flows over complex topography, and later adapted for viscoplastic fluids by Fernández-Nieto *et al.* (2023). This approach effectively eliminates numerical diffusion at stoppage, but it might still produce diffusive artefacts when the velocity is small. We found the well-balanced scheme (C4)–(C10) to be a convenient and straightforward alternative to implement.

Appendix D. The model for Bingham fluids

The model for Bingham fluids is built using the asymptotic expansions obtained in Denisenko *et al.* (2023), which possess non-zero shearing in the pseudoplug without any parameter δ. The derivation procedure is identical to that used in § 4. The final model

https://doi.org/10.1017/jfm.2026.11662 Published online by Cambridge University Press

reads

$$\frac{\partial h}{\partial t}+\frac{\partial hU}{\partial x}=0, \tag{D1}$$

$$\begin{aligned}\frac{\partial}{\partial t}(hU)+\frac{\partial}{\partial x}\left(hU^2+\Pi\right)&=\frac{\partial}{\partial x}\frac{gh^2\cos\theta}{2}\\&=\left[gh\sin\theta(1-\hat{q}(\xi))-\frac{\tau_c}{\rho}-3\nu\frac{U}{h}\right]\left(1+\left[\hat{\beta}_1(\xi)-1\right]f(1,\varphi,\xi)\right)\\&+\varphi^{-\frac{1}{2}}\left[\varphi-\hat{\alpha}(\xi)\frac{U^2}{h^2}\right]\left(\frac{7\sqrt{5}}{2}+\left[\hat{\beta}_2(\xi)-\frac{7\sqrt{5}}{2}\right]f(1,\varphi,\xi)\right),\end{aligned} \tag{D2}$$

$$\begin{aligned}\frac{h^2}{2}\left(\frac{\partial h\varphi}{\partial t}+\frac{\partial hU\varphi}{\partial x}\right)&=U\left[gh\sin\theta(1-\hat{q}(\xi))-\frac{\tau_c}{\rho}-3\nu\frac{U}{h}\right]\hat{r}_1(\xi)f(1,\varphi,\xi)\\&+U\varphi^{-\frac{1}{2}}\left[\varphi-\hat{\alpha}(\xi)\frac{U^2}{h^2}\right]\left(\frac{-7\sqrt{5}}{3}+\left[\hat{r}_2(\xi)+\frac{7\sqrt{5}}{3}\right]f(1,\varphi,\xi)\right),\end{aligned} \tag{D3}$$

where the coefficients $\hat{\beta}_1$, $\hat{\beta}_2$, $\hat{r}_1$, $\hat{r}_2$, $\hat{q}$ and $\hat{\alpha}$ are given as

$$\hat{\beta}_1(\xi)=\frac{7\xi(\xi+1)(\xi(\xi+5)+2)(\xi(23\xi+28)+12)}{6(1-\xi)(\xi+2)(21\xi^4+126\xi^3+126\xi^2+61\xi+16)}, \tag{D4}$$

$$\hat{r}_1(\xi)=-\frac{7\xi\left(\xi^2+\xi+4\right)(\xi(\xi+5)+2)(\xi(15\xi+13)+8)}{12\left(\xi^2+\xi-2\right)^2(21\xi^4+126\xi^3+126\xi^2+61\xi+16)}, \tag{D5}$$

$$\hat{\beta}_2(\xi)=\frac{7\sqrt{5}(\xi+1)\sqrt{5\xi+4}(\xi(23\xi+28)+12)}{3(1-\xi)(21\xi^4+126\xi^3+126\xi^2+61\xi+16)}, \tag{D6}$$

$$\hat{r}_2(\xi)=-\frac{7\sqrt{5}\sqrt{5\xi+4}\left(\xi^2+\xi+4\right)(\xi(15\xi+13)+8)}{6(\xi-1)^2(\xi+2)(21\xi^4+126\xi^3+126\xi^2+61\xi+16)}, \tag{D7}$$

$$\hat{q}(\xi)=\frac{\xi}{2}(1-\xi^2),\quad \hat{\alpha}(\xi)=\frac{5\xi+4}{5(\xi+2)^2}, \tag{D8}$$

and the transition function f is defined in (4.27). The critical Reynolds number for this model coincides with the result obtained in Denisenko *et al.* (2023) and is given by

$$Re_c=\frac{5\cot\theta}{2(1-Bi)}\frac{1}{1+Bi+Bi^2+Bi^3/4-Bi^4/4}. \tag{D9}$$

Appendix E. The model for power-law fluids

The model for power-law fluids is obtained from the system (4.33)–(4.35) by setting $\tau_c=0$ and $\delta=0$. This yields the following system:

$$\frac{\partial h}{\partial t}+\frac{\partial hU}{\partial x}=0, \tag{E1}$$

$$\begin{aligned}\frac{\partial}{\partial t}(hU)+\frac{\partial}{\partial x}\left(hU^2+\Pi\right)&=-\frac{\partial}{\partial x}\frac{gh^2\cos\theta}{2}\left[gh\sin\theta-\alpha_1(n)\nu\frac{U}{h}\left|\frac{U}{h}\right|^{n-1}\right]\\&+\varphi^{\frac{n-2}{2}}\left[\varphi-\alpha_2^*(n)\frac{U^2}{h^2}\right]\beta_2^*(n),\end{aligned} \tag{E2}$$

https://doi.org/10.1017/jfm.2026.11662 Published online by Cambridge University Press

$$\frac{h^2}{2}\left(\frac{\partial h\varphi}{\partial t}+\frac{\partial hU\varphi}{\partial x}\right)=U\left[gh\sin\theta-\alpha_1(n)\nu\frac{U}{h}\left|\frac{U}{h}\right|^{n-1}\right]r_1^*(n)$$
$$+U\varphi^{\frac{n-2}{2}}\left[\varphi-\alpha_2^*(n)\frac{U^2}{h^2}\right]r_2^*(n). \tag{E3}$$

The functions α_1, α_2^*, β_2^*, r_1^* and r_2^* are defined in § 4. Note that this model is applicable for any values of n.

Appendix F. The model with an alternative friction term

Instead of considering a viscous friction term proportional to $\alpha_1(n)(U/h)\,|U/h|^{n-1}$ as in the model (4.33)–(4.35), an alternative consistent model can be built with a viscous friction term linearly dependent on U. The derivation procedure is similar to that presented in § 4. In dimensional variables, this alternative model reads

$$\frac{\partial h}{\partial t}+\frac{\partial hU}{\partial x}=0, \tag{F1}$$

$$\frac{\partial}{\partial t}(hU)+\frac{\partial}{\partial x}\left(hU^2+\Pi\right)=\frac{\partial}{\partial x}\frac{gh^2\cos\theta}{2}$$
$$=\left[gh\sin\theta(1-\tilde q(n,\xi))-\frac{\tau_c}{\rho}-\frac{\nu\,\alpha_1^{\frac{1}{n}}(n)}{(g\sin\theta)^{1-\frac{1}{n}}}\frac{U}{h^{\frac{1}{n}}}\right]\left(n+\left[\beta_1(n,\xi,\zeta)\,j(n,\xi)-n\right]f(n,\varphi,\xi)\right)$$
$$+\varphi^{\frac{n-2}{2}}\left[\varphi-\alpha_2(n,\xi)\frac{U^2}{h^2}\right]\left(\beta_2^*(n)+\left[\beta_2(n,\xi,\zeta)-\beta_2^*(n)\right]f(n,\varphi,\xi)\right), \tag{F2}$$

$$\frac{h^2}{2}\left(\frac{\partial h\varphi}{\partial t}+\frac{\partial hU\varphi}{\partial x}\right)=$$
$$=U\left[gh\sin\theta(1-\tilde q(n,\xi))-\frac{\tau_c}{\rho}-\frac{\nu\,\alpha_1^{\frac{1}{n}}(n)}{(g\sin\theta)^{1-\frac{1}{n}}}\frac{U}{h^{\frac{1}{n}}}\right]r_1(n,\xi,\zeta)f(n,\varphi,\xi)\,j(n,\xi)$$
$$+U\varphi^{\frac{n-2}{2}}\left[\varphi-\alpha_2(n,\xi)\frac{U^2}{h^2}\right]\left(r_2^*(n)+\left[r_2(n,\xi,\zeta)-r_2^*(n)\right]f(n,\varphi,\xi)\right), \tag{F3}$$

where the functions $\tilde q$ and j are given by

$$\tilde q(n,\xi)=(1-\xi)\left[1-\frac{(1-\xi)^{\frac{1}{n}}(n\xi+n+1)}{n+1}\right], \tag{F4}$$

$$j(n,\xi)=n(1-\xi)^{n-\frac{1}{n}}\left(\frac{n+1}{\xi n+n+1}\right)^{1-n}. \tag{F5}$$

Other functions in (F1)–(F3) are the same as in the model (4.33)–(4.35). As a result, the replacement of the expression for the friction term leads to changes only in the first relaxation terms, while the second relaxation terms are unchanged in both the momentum and the enstrophy equations.

https://doi.org/10.1017/jfm.2026.11662 Published online by Cambridge University Press

References

ANCEY, C. 2007 Plasticity and geophysical flows: a review. *J. Non-Newtonian Fluid Mech.* **142** (1-3), 4–35.

ANCEY, C., ANDREINI, N. & EPELY-CHAUVIN, G. 2012 Viscoplastic dambreak waves: review of simple computational approaches and comparison with experiments. *Adv. Water Resour.* **48**, 79–91.

ANCEY, C. & COCHARD, S. 2009 The dam-break problem for Herschel–Bulkley viscoplastic fluids down steep flumes. *J. Non-Newtonian Fluid Mech.* **158** (1–3), 18–35.

ANDREINI, N., EPELY-CHAUVIN, G.ËL & ANCEY, C. 2012 Internal dynamics of Newtonian and viscoplastic fluid avalanches down a sloping bed. *Phys. Fluids* **24**, 79–91.

BALMFORTH, N.J. & CRASTER, R.V. 1999 A consistent thin-layer theory for Bingham plastics. *J. Non-Newtonian Fluid Mech.* **84** (1), 65–81.

BALMFORTH, N.J. & LIU, J.J. 2004 Roll waves in mud. *J. Fluid Mech.* **519**, 33–54.

BALMFORTH, N.J., CRASTER, R.V., RUST, A.C. & SASSI, R. 2006 Viscoplastic flow over an inclined surface. *J. Non-Newtonian Fluid Mech.* **139** (1–2), 103–127.

BALMFORTH, N.J., FRIGAARD, I.A. & OVARLEZ, G. 2014 Yielding to stress: recent developments in viscoplastic fluid mechanics. *Annu. Rev. Fluid Mech.* **46**, 121–146.

BENNEY, D.J. 1966 Long waves on liquid films. *J. Math. Phys.* **45** (1-4), 150–155.

BIRD, R.B., DAI, G.C., YARUSSO, B.J. & BIRD, R.B. 1983 The rheology and flow of viscoplastic materials. *Rev. Chem. Engng* **1** (1), 1–70.

BOUCHUT, F. 2005 *Nonlinear Stability of Finite Volume Methods for Hyperbolic Conservation Laws: and Well-Balanced Schemes for Sources*. Birkhäuser Basel.

BOUTOUNET, M., MONNIER, J. & VILA, J.-P. 2016 Multi-regime shallow free surface laminar flow models for quasi-Newtonian fluids. *Eur. J. Mech. B* **55**, 182–206.

CHAMBON, G., FREYDIER, P., NAAIM, M. & VILA, J.-P. 2020 Asymptotic expansion of the velocity field within the front of viscoplastic surges: comparison with experiments. *J. Fluid Mech.* **884**, A43.

CHAMBON, G., GHEMMOUR, A. & LAIGLE, D. 2009 Gravity-driven surges of a viscoplastic fluid: an experimental study. *J. Non-Newtonian Fluid Mech.* **158** (1–3), 54–62.

CHESNOKOV, A. 2021 Formation and evolution of roll waves in a shallow free surface flow of a power-law fluid down an inclined plane. *Wave Motion* **106**, 102799.

COUSSOT, P. 1994 Steady, laminar, flow of concentrated mud suspensions in open channel. *J. Hydraul. Res.* **32** (4), 535–559.

COUSSOT, P. 1997 *Mudflow Rheology and Dynamics*. Balkema.

DELEAGE, E. & RICHARD, G.L. 2025 A depth-averaged model for granular flow consistent with the incompressible $\mu(i)$ rheology. *J. Fluid Mech.* **1009**, A57.

DENISENKO, D., RICHARD, G. & CHAMBON, G. 2023 A consistent three-equation shallow-flow model for Bingham fluids. *J. Non-Newtonian Fluid Mech.* **321**, 4–35.

DENISENKO, D., RICHARD, G.L. & CHAMBON, G. 2025 Smooth thin-layer asymptotic expansions for free-surface yield-stress flows. *J. Non-Newtonian Fluid Mech.* **344**, 105456.

DIMAKOPOULOS, Y., PAVLIDIS, M. & TSAMOPOULOS, J. 2013 Steady bubble rise in Herschel–Bulkley fluids and comparison of predictions via the Augmented Lagrangian Method with those via the Papanastasiou model. *J. Non-Newtonian Fluid Mech.* **200**, 34–51.

DUBASH, N., BALMFORTH, N.J., SLIM, A.C. & COCHARD, S. 2009 What is the final shape of a viscoplastic slump? *J. Non-Newtonian Fluid Mech.* **158** (1), 91–100.

FERNÁNDEZ-NIETO, E.D., NOBLE, P. & VILA, J.-P. 2010 Shallow water equations for non-Newtonian fluids. *J. Non-Newtonian Fluid Mech.* **165** (13-14), 712–732.

FERNÁNDEZ-NIETO, E.D., GARRES-DÍAZ, J. & VIGNEAUX, P. 2023 Multilayer models for hydrostatic Herschel-Bulkley viscoplastic flows. *Comput. Math. Appl.* **139**, 99–117.

FIOROT, G.H., DA ROCHO, V., MÖLLER, S.V., PEREIRA, JÃO B., DA CUNHA, E.F. & DE MACIEL, G. 2024 An experimental assessment of roll waves evolution in mud-like fluids flowing down steep slopes. *J. Braz. Soc. Mech. Sci. Engng* **46**, 483.

FRIGAARD, I.A. & NOUAR, C. 2005 On the usage of viscosity regularisation methods for visco-plastic fluid flow computation. *J. Non-Newtonian Fluid Mech.* **127** (1), 1–26.

GLOWINSKI, R. & WACHS, A. 2011 On the numerical simulation of viscoplastic fluid flow. In *Handbook of Numerical Analysis*, vol. 16, pp. 483–717. Elsevier.

HOGG, A.J. & MATSON, G.P. 2009 Slumps of viscoplastic fluids on slopes. *J. Non-Newtonian Fluid Mech.* **158** (1), 101–112.

HOGG, A.J. & PRITCHARD, D. 2004 The effects of hydraulic resistance on dam-break and other shallow inertial flows. *J. Fluid Mech.* **501**, 179–212.

HUANG, X. & GARCIA, M.H. 1998 A Herschel–Bulkley model for mud flow down a slope. *J. Fluid Mech.* **374**, 305–333.

https://doi.org/10.1017/jfm.2026.11662 Published online by Cambridge University Press

KALLIADASIS, S., RUYER-QUIL, C., SCHEID, B. & VELARDE, M.G.ÍA 2012 *Falling Liquid Films*, vol. 176. Springer Science & Business Media.

LIU, Y., BALMFORTH, N.J. & HORMOZI, S. 2019 Viscoplastic surges down an incline. *J. Non-Newtonian Fluid Mech.* **268**, 1–11.

MUCHIRI, D.K., HEWETT, J.N., SELLIER, M., MOYERS-GONZALEZ, M. & MONNIER, J. 2024 Numerical simulations of dam-break flows of viscoplastic fluids via shallow water equations. *Theor. Comput. Fluid Dyn.* **38**, 557–581.

MUCHIRI, D.K., MONNIER, J. & SELLIER, M. 2025 Derivation and numerical resolution of 2D shallow water equations for multi-regime flows of Herschel–Bulkley fluids. *Eur. J. Mech. B* **109**, 22–36.

NG, C.-O. & MEI, C.C. 1994 Roll waves on a shallow layer of mud modelled as a power-law fluid. *J. Fluid Mech.* **263**, 151–184.

NOBLE, P. & VILA, J.-P. 2013 Thin power-law film flow down an inclined plane: consistent shallow-water models and stability under large-scale perturbations. *J. Fluid Mech.* **735**, 29–60.

MOUNKAILA NOMA, D., DAGOIS-BOHY, S., MILLET, S., BOTTON, V., HENRY, D. & BEN HADID, H. 2021 Primary instability of a visco-plastic film down an inclined plane: experimental study. *J. Fluid Mech.* **922**, R2.

OOSHIDA, T. 1999 Surface equation of falling film flows with moderate Reynolds number and large but finite Weber number. *Phys. Fluids* **11** (11), 3247–3269.

PASTOR, M., QUECEDO, M., GONZÁLEZ, E., HERREROS, M.I., MERODO, J.A. & MIRA, P.2004 Simple approximation to bottom friction for Bingham fluid depth integrated models. *J. Hydraul. Engng* **130**, 149–155.

PUMIR, A., MANNEVILLE, P. & POMEAU, Y. 1983 On solitary waves running down an inclined plane. *J. Fluid Mech.* **135**, 27–50.

RICHARD, G.L. 2024 Roll waves in a predictive model for open-channel flows in the smooth turbulent case. *J. Fluid Mech.* **983**, A31.

RICHARD, G.L., RUYER-QUIL, C. & VILA, J.-P. 2016 A three-equation model for thin films down an inclined plane. *J. Fluid Mech.* **804**, 162–200.

RICHARD, G.L. & GAVRILYUK, S.L. 2012 A new model of roll waves: comparison with Brock's experiments. *J. Fluid Mech.* **698**, 374–405.

RICHARD, G.L. & GAVRILYUK, S.L. 2013 The classical hydraulic jump in a model of shear shallow-water flows. *J. Fluid Mech.* **725**, 492–521.

RICHARD, G.L., GISCLON, M., RUYER-QUIL, C. & VILA, J.P. 2019 Optimization of consistent two-equation models for thin film flows. *Eur. J. Mech. B* **76**, 7–25.

RUYER-QUIL, C., CHAKRABORTY, S. & DANDAPAT, B.S. 2012 Wavy regime of a power-law film flow. *J. Fluid Mech.* **692**, 220–256.

RUYER-QUIL, C. & MANNEVILLE, P. 2000 Improved modeling of flows down inclined planes. *Eur. Phys. J. B* **15**, 357–369.

SAINGIER, G., DEBOEUF, S. & LAGRÉE, P.-Y. 2016 On the front shape of an inertial granular flow down a rough incline. *Phys. Fluids* **28** (5), 053302.

TESHUKOV, V.M. 2007 Gas-dynamic analogy for vortex free-boundary flows. *J. Appl. Mech. Tech. Phys.* **48**, 303–309.

TORO, E.F. 1999 *Riemann Solvers and Numerical Methods for Fluid Dynamics*. Springer.

USHA, R. & UMA, B. 2004 Modeling of stationary waves on a thin viscous film down an inclined plane at high Reynolds numbers and moderate Weber numbers using energy integral method. *Phys. Fluids* **16** (7), 2679–2696.

https://doi.org/10.1017/jfm.2026.11662 Published online by Cambridge University Press